

University of Konstanz  
Department of Computer and Information Science

Master Thesis for the degree  
Master of Science (M.Sc.) in Information Engineering

# **Acquisition, Processing, and Analysis of Pedal Motion Data in Bicycling**

by

**Julia Blumenthal**

(Matriculation number: 01/526959)

1<sup>st</sup> Referee: Prof. Dr. Dietmar Saupe  
2<sup>nd</sup> Referee: Prof. Dr. Ulrik Brandes  
Supervisor: Thorsten Dahmen

Konstanz, April 10, 2009

## **Acknowledgement**

I would like to thank the staff at the Radlabor Freiburg (Radlabor GmbH, Freiburg, Germany) for the use of the laboratory facilities and for providing assistance with the measurement devices.

## **Abstract**

In cycling, force applied to the pedal is conventionally measured using strain gauges or piezoelectric force transducers within the pedal body or at the crank. This thesis takes a different approach to determine pedal force based on motion capturing.

Pedal force is calculated as the sum of forces needed to overcome the resistance of the ergometer brake and the moment of inertia of the ergometer's flywheel. The former is obtained from cadence and power measurements of the ergometer, the latter by means of flywheel inertia and angular acceleration of the crank.

The crank angle was determined by tracking the pedal movement using motion capturing. Then the second derivative of the crank angle gave its angular acceleration. As noise inherent in measurement data causes serious problems when computing derivatives, the data was smoothed beforehand. Three smoothing techniques were applied: a Butterworth filter, a Kalman smoother, and singular spectrum analysis. The angular acceleration obtained by the three methods was similar.

The analysis of the pedal motion data revealed that systematic errors and strong measurement noise prevent sufficiently accurate estimates of the angular acceleration of the crank. Therefore, the resulting pedal force estimates differ considerably from the force obtained by a pedal force measurement device (Powertec System).

## Kurzfassung

Im Radsport werden auf die Pedale ausgeübte Kräfte meist mit Dehnmessstreifen oder piezoelektrischen Kraftaufnehmern gemessen. In der vorliegenden Masterarbeit wird ein anderer Ansatz, basierend auf der Erfassung von Bewegungsdaten (engl. Motion Capturing), verfolgt.

Die Pedalkraft wird als Summe der Kräfte berechnet, die aufgebracht werden müssen, um den Widerstand der Ergometerbremse und des Trägheitsmoments des Ergometer-Schwungrads zu überwinden. Ersteres wird mittels der vom Ergometer gemessenen Trittfrequenz und Leistung bestimmt, letzteres basierend auf der Trägheit des Schwungrads und der Winkelbeschleunigung der Kurbel.

Die Kurbelwinkel werden anhand der Pedalbewegung berechnet, die mittels Motion Capturing erfasst wird. Die zweite Ableitung der Kurbelwinkel ergibt die Winkelbeschleunigung. Da die Berechnung von Ableitungen auf verrauschten Messdaten sehr problematisch ist, werden die Daten vorab geglättet. Dazu wurden drei verschiedene Verfahren angewandt: ein Butterworth Filter, ein Kalman Smoother und Singular Spectrum Analysis. Die ermittelten Winkelbeschleunigungen aller drei Methoden waren ähnlich.

Die Analyse der Pedal-Bewegungsdaten zeigt, dass systematische Fehler und starkes Messrauschen eine ausreichend genaue Schätzung der Winkelbeschleunigung der Kurbel verhindern. Deshalb weichen die resultierenden Pedalkraftschätzungen beträchtlich von den mittels eines Kraftmessgeräts (Powertec System) gemessenen Pedalkräften ab.

# Contents

<b>1</b>	<b>Introduction</b>	<b>1</b>
1.1	Analysis of Pedal Force . . . . .	1
1.2	Pedal Force Determination Based on Motion Data . . . . .	2
1.3	Derivative Estimation of Motion Data . . . . .	3
1.4	Outline . . . . .	5
<b>2</b>	<b>Pedal Forces and Ergometer Cycling</b>	<b>6</b>
2.1	Basics of Pedal Force . . . . .	6
2.1.1	Types of Pedal Force . . . . .	6
2.1.2	Propagation of Pedal Force in Bicycling . . . . .	8
2.2	Ergometer Cycling . . . . .	9
2.2.1	Inertia in Ergometer Cycling . . . . .	10
2.2.2	Propagation of Force in Ergometer Cycling . . . . .	10
2.2.3	Variations of Braking Force . . . . .	11
<b>3</b>	<b>Data Acquisition</b>	<b>14</b>
3.1	Measuring Instruments . . . . .	14
3.1.1	LUKOtronic Motion Capture System . . . . .	14
3.1.2	SRM Ergometer . . . . .	16
3.1.3	SRM Training System . . . . .	16
3.1.4	Powertec . . . . .	17
3.2	Experimental Setup . . . . .	18
3.3	Series of Measurements . . . . .	19
<b>4</b>	<b>Pedal Force Computation</b>	<b>21</b>
4.1	Braking Force . . . . .	22
4.2	Inertial Force . . . . .	23
4.3	Powertec Pedal Force . . . . .	25
4.4	Synchronisation . . . . .	25
<b>5</b>	<b>Crank Angular Acceleration</b>	<b>27</b>
5.1	Problems Affecting Derivative Estimation . . . . .	27
5.1.1	Measurement Noise . . . . .	27
5.1.2	Instrumental Error . . . . .	38
5.2	Preprocessing of Motion Data . . . . .	40
5.2.1	Determination of Least Squares Plane . . . . .	40
5.2.2	Transformation into 2D Coordinate System . . . . .	42
5.3	Smoothing . . . . .	42
5.3.1	Amplitude Spectrum . . . . .	44

*Contents*

---

5.3.2	Butterworth Filter . . . . .	45
5.3.3	Kalman Smoother . . . . .	47
5.3.4	Singular Spectrum Analysis . . . . .	51
5.4	Derivative Estimation . . . . .	54
5.4.1	Angular Position . . . . .	54
5.4.2	First and Second Derivatives . . . . .	56
<b>6</b>	<b>Results and Discussion</b>	<b>57</b>
6.1	Angular Velocity and Acceleration . . . . .	57
6.1.1	Examination of Exemplary Measurement . . . . .	57
6.1.2	Dependency on Power and Cadence . . . . .	61
6.2	Pedal Force Estimates . . . . .	62
6.2.1	Two Major Force Peaks . . . . .	63
6.2.2	Further Minor Force Peaks . . . . .	64
6.2.3	Braking Force . . . . .	65
6.2.4	Phase Lag . . . . .	65
<b>7</b>	<b>Conclusions</b>	<b>66</b>
7.1	Summary . . . . .	66
7.2	Outlook . . . . .	67
	<b>List of Figures</b>	<b>69</b>
	<b>Bibliography</b>	<b>71</b>

# 1 Introduction

Motion capturing is used in entertainment for movies and computer games. In medical care it is employed for diagnosis and therapy of diseases. Moreover, it is used in serious sport for analysing and improving courses of movements to gain performance enhancements or rehabilitation.

The topic of this thesis is to determine the pedal force applied during ergometer cycling by means of the crank movement, which is recorded by a motion capture system.

## 1.1 Analysis of Pedal Force

Motivations behind analysing pedal forces shall be pointed out, followed by a short review of employed measurement devices.

### Purpose

An aim of optimising a cyclist's performance is to maximise the proportion of expended energy that is made available for thrust [HMH01]. The motion of a bicycle is mainly due to the pedal forces applied by the cyclist, besides other forces like gravity, inertia and wind energy [Gre05]. Hence, the analysis of the pedalling technique is one of the starting points for increasing performance in cycling.

Popularly, a smooth pedalling technique that involves pushing or pulling at all stages during a crank revolution and which results in an even force at all crank positions is advised [Gre05, HSS<sup>+</sup>98]. Obviously, pulling up is only possible if clipless pedals are used. This technique seems desirable, as the steady application of force during the crank revolution makes use of the exerted force in the most efficient way.

Measuring pedal forces allows to investigate to what extent a cyclist accomplishes this technique. Empirical studies show that cyclists rarely pull up during upstroke [CS86]. It is assumed that it is uneconomical to do so and instead unloading the pedal during upstroke is advised.

Another important issue concerning the pedalling technique is the identification of force asymmetries between both legs. Large asymmetries probably cause a poorer performance and hence should be removed [CS86]. Further, it might be of interest, if or how pedal force profiles change when a cyclist

becomes exhausted. Moreover, analysing pedal forces is useful for the comparison of different shoe-pedal interfaces.

The analysis of force applied to the pedal demands for measurement devices providing precise force information at all stages during a pedal cycle, which means, with a high sampling rate (usually  $\geq 40$  Hz) or angular resolution regarding the crank position.

### **Pedal Force Measurement Instruments**

Pedal force measurement attempts date back until 1889, when 'R. P. Scott made the first force-measuring pedal, which was fitted to the large wheeled "ordinary bicycle" of the day' [FC78, p. 90].

Often pedal force measurement is instrumented into the pedal-body and is based on strain gauges [HD81, NHZ88] or piezoelectric force transducers [BG90]. Others placed strain gauges at the pedal spindle shaft outboard of the crank [AV96]. For reviews of pedal force measurement devices it is referred to [GBR91] and [Bro03].

The operation principle of those devices is based on the mechanical deflection caused by the force applied to the pedal. This deflection results in a proportional change in resistance. The resistance can be captured by means of current and voltage measurements, which are then used to compute the respective force.

To measure force in two or three directions several force transducers are installed orthogonal to each other. Most devices determine force relative to the pedal. Then, additionally the angle of the pedal with respect to the crank is tracked to allow conversion of those measured forces into their components normal and tangential to the crank.

A more recent development is the Powertec System presented by Stapelfeldt et al. [SMO<sup>+</sup>07]. It uses Hall effect sensor systems to measure forces radial and tangential to the crank separately for the left and right foot. The Powertec System is used for the evaluation of our force determination attempt by means of motion capturing.

Evidence of other pedal force measurement approaches based on motion capturing could not be found. However, a related approach to determine pedal force (to be precise, pedal torque) was followed by Lakomy [Lak93], who computed the torque applied to the pedals of a friction-loaded cycle ergometer by means of the flywheel acceleration. To monitor the flywheel speed a small electric generator driven by the flywheel was used.

## **1.2 Pedal Force Determination Based on Motion Data**

Pedal force measurement devices are not widely available, but mainly self-constructions of scientific institutions [Sta06]. Our university department does not own such a device and those are quite expensive.

However, a LUKOtronic (LUKOtronic Lutz-Kovacs-Electronics OEG., Innsbruck, Austria) motion capture system and a Cyclus 2 (RBM Elektronik, Automation, Leipzig, Germany) cycling ergometer are available. This ergometer only provides information about average power and cadence per pedal revolution at a sampling rate of 2 Hz, but a higher resolution is needed for a detailed analysis of pedal forces.

An approach is made to determine pedal force with a high angular resolution by tracking the motion of the pedal. We attempt to compute the pedal force as the sum of forces needed to overcome braking resistance and the moment of inertia of the flywheel.

Therefore, the braking resistance is calculated from the power and cadence measurements of the ergometer. Further, the inertial force of the flywheel is determined by means of the angular acceleration of the crank, which is obtained using motion capturing.<sup>1</sup>

For this study an SRM (Schoberer Rad Meßtechnik SRM GmbH, Jülich, Germany) ergometer was used.<sup>2</sup>

Our method for obtaining pedal force is based on the torque which causes the motion of the crank. Hence, it is restricted to the part of the force that is tangential to the crank. Radial and lateral forces (which do not result in crank motion) cannot be determined. Likewise, it is not possible to specify which portion of the computed pedal force is due to the left or the right foot.

### 1.3 Derivative Estimation of Motion Data

A crucial point regarding the pedal force computation is to identify an appropriate estimation of the acceleration of the crank based on its captured motion (i.e., determining the second derivative).

This problem is caused by noise contained in the signal, which is referred to as measurement noise. It arises from the finite spatial precision of the measurement devices and the digitisation process and it is assumed to be additive, wide-band, and white.

Another type of errors are systematic ones, like wrong marker placements or deformations of material. For the derivative computation they are less problematic.

Derivative estimation of experimental data is highly sensitive to noise [LRS86]. Although noise might not be noticeable in the spatial trajectories of motion data, it severely affects the derivatives (see, for example, [Win90, Wol95]).

---

<sup>1</sup> With respect to the chosen sampling rate of 295 Hz, the inertial force is captured with an angular resolution of about  $2^\circ$  (with regards to a cadence of 100 rpm), resulting in the same resolution for the total computed pedal force.

<sup>2</sup> Even though the SRM System provides power information, this data is not sufficient for a detailed analysis of the pedal force. Besides the fact that the delivered data are mean values per crank revolution, they are sampled with a frequency of 2 Hz. Depending on the cadence this results in about one or two values per crank revolution. Hence, it does not allow an analysis of the variations of the pedal force within a crank cycle.

This becomes easily evident when considering that computation of the  $n$ -th derivative in the time domain corresponds to a multiplication with  $(i\omega)^n$  in the frequency domain, where  $i$  denotes the imaginary unit ( $i^2 = -1$ ),  $\omega = 2\pi f$  the angular frequency and  $f$  the frequency.

Therefore, within the captured motion trajectories high-frequency noise with small amplitudes might be not perceptible. When computing the velocity these small amplitudes are multiplied with their high frequencies, or in case of acceleration even with their squared frequencies. Consequently, due to this high-frequency amplification, differentiation acts as a high-pass filter, and the noise can seriously distort the computed derivatives.

Whilst noise is typically wide-band, the motion itself is often assumed to occupy only lower frequencies. To diminish the influence of noise on derivative computation, usually some kind of filtering or smoothing to remove (high-frequency) noise is applied before differentiation.

The most widely used traditional filtering techniques comprise digital low-pass Butterworth filters [WSH74] in the frequency domain and spline approximation, in particular Woltrings Spline Package GCVSPL (generalized, cross-validatory spline smoothing and differentiation)[Wol86] in the time domain. Others are based on fourier series [AB74, Hat81]. Reviews of traditionally used methods can be found in [Wol85, Wol95].

Techniques based on stochastic signal models were proposed, including state-space approaches like a Kalman smoother by Fioretti and Jetto [FJ89, FJ94]. Kalman smoothers (and Kalman filters in general) can perform noise removal and derivative estimation simultaneously, making use of all available information (i.e., the measurement data itself, knowledge about the measuring devices and the system) [May79]. In contrast, the other techniques mentioned above first filter out noise and then compute the derivatives.

The crucial factor common to all techniques is to define a proper degree of smoothing, to prevent noisy derivatives but to avoid oversmoothing as well. For example, this is the choice of the cutoff frequency when using Butterworth filters, the smoothing factor for spline approximations, or the values of the measurement and process noise for Kalman filtering.

The techniques mentioned above assume the signal to be stationary and work reasonably well for low-pass signals with additive white measurement noise (comparisons of several filtering techniques can inter alia be found in [PNW77, DF92, CFL93]).

When a signal is nonstationary (i.e., if its statistical or frequency characteristics change over time) traditional filtering techniques are not well-suited [Ste04]. Human kinetics are often assumed stationary, but actually impact-like activities, as heel strike in gait analysis, are nonstationary [Wol95, GSV00, GSG02].

Applying a conventional filtering technique to nonstationary data results in suboptimal acceleration estimates, depending on the chosen cutoff frequency. Either a smooth acceleration curve, not reaching the peak acceleration, can be obtained by choosing a low cutoff frequency, or peak acceleration can be

reached by means of a high cutoff frequency, but at the cost of an overall noisy acceleration [GSV00].

More recently, advanced filtering techniques were proposed to better cope with nonstationary processes, like discrete wavelet transforms [IA99], singular spectrum analysis [AS97, ADCP04, ADCP05] and the Wigner function [GSV00, GSG02]. Those techniques accommodate changing frequency characteristics within different regions of the signal by a varying level of noise suppression.

A filtering technique that was generally found to be the best does apparently not exist. Moreover, the performance of the filters depends on the particular characteristics of a signal and its noise. Even the best acceleration estimates for a specific signal, determined by comparing different techniques, often deviate noticeably from the true acceleration (for examples, see [CFL93, FJ94, GSG02]).

## 1.4 Outline

A basic introduction to pedal forces is given in Chapter 2, which covers the different types of pedal forces and the propagation of pedal force. Further, some aspects inherent to ergometer cycling are discussed, like the inertia provided by the ergometer, the propagation of pedal force in ergometer cycling and possible variations of the braking force.

In Chapter 3 the acquisition of experimental data is depicted. The employed measurement devices, the experimental setup and the accomplished measurement series are described.

The computation of pedal force based on braking and inertial force follows in Chapter 4.

Smoothing of motion data and derivative computation is dealt with in Chapter 5. Noisy data is a severe problem for the computation of derivatives. Thus, preceding the smoothing of the motion data a detailed analysis of the noise and errors affecting the measurements is accomplished. Three filtering techniques are employed for smoothing the measured data: a Butterworth filter, a Kalman smoother and singular spectrum analysis.

Finally, in Chapter 6, this approach of pedal force computation is validated by comparing the resultant force profiles with those determined by the above mentioned pedal force measurement device *Powertec System*. Furthermore, problems and elements of uncertainty effecting these results are discussed.

In the end, conclusions are drawn and recommendations for further research are pointed out (Chapter 7).

The computations accomplished in this thesis are implemented in MATLAB. The source code, measurement data and further figures can be found on the accompanying DVD.

## 2 Pedal Forces and Ergometer Cycling

This chapter gives a basic introduction to pedal forces. Section 2.1 covers the tangential and radial component of pedal force, variations of force within a pedal cycle and the propagation of force. Aspects specifically related to ergometer cycling are considered in Section 2.2.

### 2.1 Basics of Pedal Force

The next to subsections give a short insight into the types of forces applied to the pedal (Section 2.1.1) and its propagation (Section 2.1.2).

#### 2.1.1 Types of Pedal Force

The *resultant force*  $F_{res}$  exerted on the pedal can be divided into two parts regarding their direction towards the crank: the *tangential component*  $F_t$  and the *radial component*  $F_r$  (see Figure 2.1). The tangential force acts perpendicular to the crank and it is responsible for the movement of the crank and consequently the bicycle. Thus, it is also called *effective component*. The radial force acts parallel to the crank, which means it minimally lengthens or compresses the crank, not perceptible for the human eye. Since it does not contribute to the movement of the crank, it is referred to as the *ineffective component*.

Figure 2.2 shows the resultant force one foot applies to the pedal during a crank revolution and the respective pedal orientation. At the top dead centre (crank angle zero), rarely force is applied. Up to about a crank angle of  $120^\circ$ , the rider pushes downward and forward and the magnitude of the resultant force increases. Afterwards, it is pushed downward and backward until about  $310^\circ$ .

During the second half of the downstroke the resulting force is still quite large. However, due to its orientation its efficient (i.e., tangential) part decreases. Pulling-up during upstroke can hardly be noticed. For a more detailed discussion see [Bro03].

The measurement of tangential and radial forces allows the separation between effective force, that is force made available for thrust, and ineffective force which seems to be wasted. Therefore, the knowledge of these forces is often seen as a base for an improvement of the effectiveness of the applied force by reducing the ineffective component.

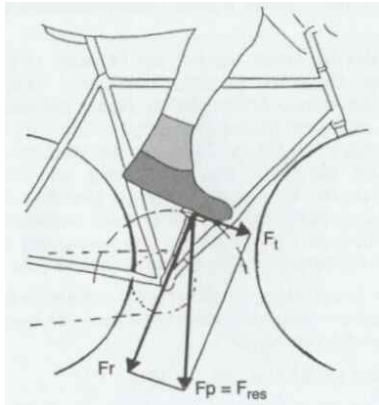


Figure 2.1: Components of force applied to the pedal:  $F_r$  = radial force,  $F_t$  = tangential force and  $F_{res}$  = resultant force. In:[Gre05, p. 195]

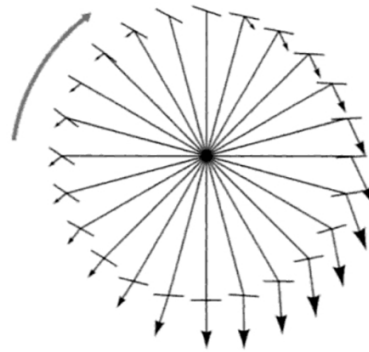


Figure 2.2: The diagram shows the magnitude and orientation of the resultant force during a pedal cycle, as well as the orientation of the pedal. In:[Bro03, p. 125]

As Broker and Gregor [BG96, p.152] stated, 'A fault exists in this logic, and the fault becomes apparent when one considers that the fundamental dynamics of the spinning leg, foot, and pedal system generate forces (measurable at the pedal) independent of muscular work, or energy cost' (also refer to [Wil04]). For example, it is easy to imagine that eliminating the radial force at the bottom of the pedal stroke (i.e., not pushing downwards), would mean an increase in required muscle work. Hence, the goal of minimising the radial force should be considered thoughtfully.

Only the tangential force is responsible for the crank torque which causes the crank revolutions [Bro03]. The crank torque varies throughout the pedal cycle, which can be divided into several phases. For a more detailed consideration of this topic it is referred to [HMH01].

A typical torque profile exhibits a high and positive crank torque during downstroke and a negative torque during upstroke. This means the foot is rather resting on the pedal than pulling during upstroke. At the top and bottom dead centre the torque is low. Figure 2.3 shows a characteristic torque profile for the net torque (Figure 2.3(a)), which is the sum of the torque of both feet, and the torque contributions separately for the left and right foot (Figure 2.3(b)).

Asymmetries between both legs, as existent in the mentioned figure, are quite common [FC78]. Each of the two torque peaks during a pedal cycle reflects the downstroke of one leg and the upstroke of the other. For most cyclists, the magnitude of those two torque peaks differs due to at least slight asymmetries between both legs.

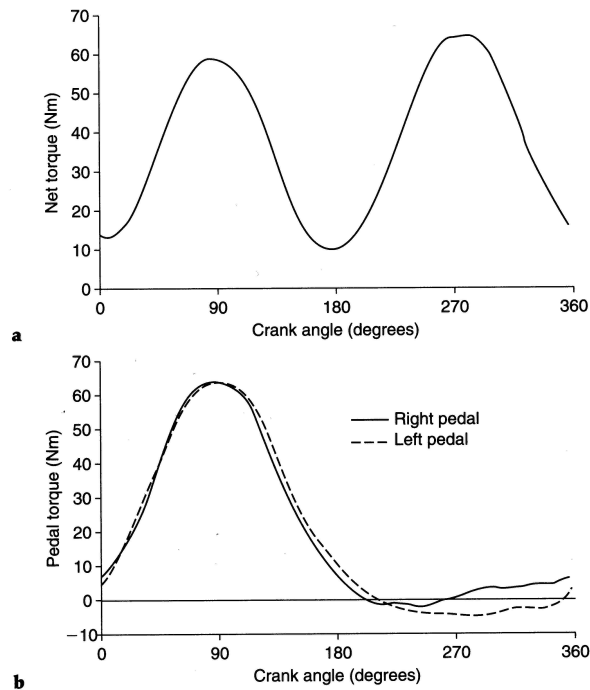


Figure 2.3: (a) Net crank torque profile (of both legs) and (b) Crank torque profiles of left and right leg separately (pedal cycle starting from top dead centre). In:[Bro03, p. 127]

### 2.1.2 Propagation of Pedal Force in Bicycling

Forces expended at the upper part of the body play a significant role for the overall achievement of a cyclist. Nonetheless, concerning propulsion of the bike, the amount of tangential force applied to the pedal is the decisive factor, no matter how it was produced by the interaction of muscles all over the body.

The propagation of the force from the pedal to the wheel (refer to [Gre05, CS86]) is outlined in Figure 2.4. The tangential force  $F_1$  that the cyclist applies to the pedal causes a torque  $\tau_1$  about the crank axis. The magnitude of a torque is defined as the product of the force and the length of the lever arm, here denoted as  $L_1$ . Thus it follows:

$$\tau_1 = F_1 \cdot L_1 . \quad (2.1)$$

The sprockets and the chain act as a torque converter. In cycling a low speed and a high torque at the crank are usually converted to a higher speed with a smaller torque at the rear sprocket.

The force  $F_2$  in the chain multiplied by the radius of the front sprocket  $L_2$  equals  $\tau_1$ . Thus,  $F_2$  can be obtained from

$$F_2 = F_1 \cdot \frac{L_1}{L_2} . \quad (2.2)$$

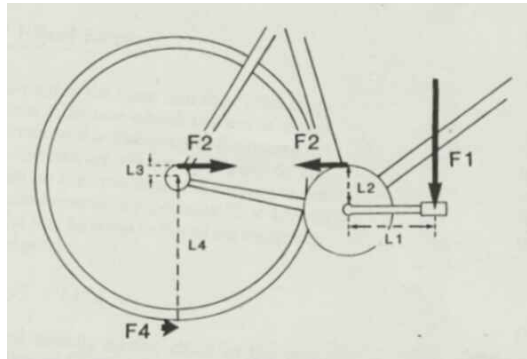


Figure 2.4: Propagation of tangential force from the pedal to the wheel. Force  $F_4$  denotes the force exerted by the road on the tire, which is in the opposite direction to the force applied by the wheel on the road. In:[CS86, p. 99]

Then the torque  $\tau_2$  at the rear is defined by the product of  $F_2$  and the radius of the rear sprocket  $L_3$ :

$$\tau_2 = F_2 \cdot L_3 . \quad (2.3)$$

Besides,  $\tau_2$  can be determined by means of the force applied to the wheel  $F_4'$  and the wheel radius  $L_4$ :

$$\tau_2 = F_4' \cdot L_4 . \quad (2.4)$$

Hence, using (2.2), (2.3) and (2.4), for the force  $F_4'$  at the wheel it follows

$$F_4' = F_2 \cdot \frac{L_3}{L_4} = F_1 \cdot \frac{L_1}{L_2} \cdot \frac{L_3}{L_4} . \quad (2.5)$$

In reality, force transmission is not perfect, due to friction losses in the internal machinery as the chain, gear train and bearing. Those losses are rather a minor factor. According to Gregor et al. they make up less than 5% of the overall resistive forces [GBR91]. Kyle denotes the amount of power input lost due to friction by 3% to 5% [Kyl86]. For an overview concerning transmission efficiency it is referred to [Wil04].

## 2.2 Ergometer Cycling

Studies regarding cycling are often conducted in a laboratory by simulating road cycling by means of cycling ergometers. As this thesis deals with pedal force, in the following some aspects related to forces on ergometers will be considered.

Section 2.2.1 investigates the simulation of real world inertia in ergometer cycling. Subsequently, the propagation of pedal force based on inertial force

<sup>1</sup>In Figure 2.4, a force  $F_4$  denotes the force exerted by the road on the tire. Therefore, the opposed force which is applied by the wheel on the road is named  $F_4'$ .

and braking force is depicted in Section 2.2.2. Finally, in Section 2.2.3 the power measurements of the SRM ergometer used in this study are analysed with respect to the amount of variation of the underlying braking force.

### 2.2.1 Inertia in Ergometer Cycling

In outdoor cycling criteria like air resistance, rolling resistance, or the weight of the rider bicycle combination are decisive factors regarding the mechanical power output [DPCMS79]. When cycling indoors using an ergometer, they do not apply.

Instead the resistance the cyclist has to overcome is determined by the ergometer brake and the inertia of a flywheel contained in the ergometer, which is rotated due to pedalling.

Flywheels are employed for simulating real world inertia, since they reduce crank-speed variations within a pedal cycle [FZD96, Wil04]. However, referring to Wilson [Wil04], the inertia at the crank is often as little as one-tenth of that of the rider bicycle combination.

According to Fregly et al. [FZD96], crank inertia is typically  $<6.5 \text{ kgm}^2$  during ergometer cycling and between 4 and  $11 \text{ kgm}^2$  for roller cylinders. In contrast, when cycling on the road, inertia is much higher. For instance, a rider and bicycle combination of mass 75 kg and a speed of  $40 \text{ km/h}$  has a kinetic energy of 4630 J. To simulate this kinetic energy by cycling on an ergometer at a cadence of 90 rpm, the crank inertia has to be  $104 \text{ kgm}^2$ .

The Cyclus 2 ergometer available at our university department does not allow the simulation of realistic inertia. The inertia at the crank is determined by the inertia of the flywheel and the gear ratio. For example, a gear ratio of  $53/17$  results in a crank inertia of  $5.3 \text{ kgm}^2$ .

SRM ergometers allow the simulation of real world inertia (see Section 3.1.2). For our experiments, the preset inertia at the laboratory SRM ergometer was not altered. This resulted in an inertia of  $7.5 \text{ kgm}^2$  applying to the crank, which is not realistic.

### 2.2.2 Propagation of Force in Ergometer Cycling

Obviously, in ergometer cycling force must be propagated following the same rules as in road cycling, which was discussed in Section 2.1.2. This time, propagation of force in ergometer cycling is examined in a reverse direction.

The tangential force exerted onto the pedal must have the same magnitude as the resistive forces applying to it, but in opposite direction. As pointed out earlier, this resistance is due to the brake and the inertia of the flywheel.

Figure 2.5 illustrates the propagation of force in ergometer cycling. Pedalling with a crank angular velocity  $\omega_C$  and crank angular acceleration  $\alpha_C$  causes a rotation of the flywheel with angular velocity  $\omega_F$  and angular ac-

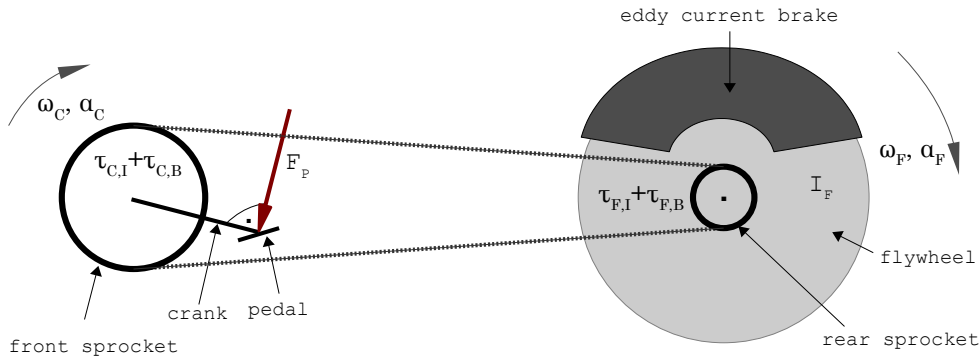


Figure 2.5: Outline of force propagation from pedal to flywheel.

celeration  $\alpha_F$ :

$$\omega_F = g \cdot \omega_C, \quad \alpha_F = g \cdot \alpha_C, \quad (2.6)$$

where  $g$  denotes the gear ratio as *teeth of front sprocket / teeth of rear sprocket*.<sup>2</sup>

The flywheel creates a torque  $\tau_{F,I}$  about its axis of rotation, which is defined by its moment of inertia  $I_F$  and its angular acceleration  $\alpha_F$ :

$$\tau_{F,I} = I_F \cdot \alpha_F. \quad (2.7)$$

Likewise, the brake causes a torque  $\tau_{F,B}$  about the axis of rotation of the rear sprocket, since it puts resistance against the motion of the flywheel.

Through the sprockets and the chain, both torques are transmitted to the crank. Those torques at the crank, denoted by  $\tau_{C,I}$  and  $\tau_{C,B}$ , are determined by

$$\tau_{C,I} = g \cdot \tau_{F,I}, \quad \tau_{C,B} = g \cdot \tau_{F,B}. \quad (2.8)$$

Then, the tangential force  $F_P$  which is exerted onto pedal is the amount of force needed to overcome both opposed torques:

$$F_P = -\frac{\tau_{C,I} + \tau_{C,B}}{l_C}, \quad (2.9)$$

where  $l_C$  denotes the length of the crank. The  $-$  ('minus') sign in (2.9) arises because of the opposite directions of the forces.

### 2.2.3 Variations of Braking Force

The SRM ergometer used in this study provides braking force by means of an eddy current brake. The resistance of an eddy current brake depends on the current supplied to it and the angular velocity of the flywheel.

<sup>2</sup>Usually gear ratios are defined by *teeth of rear sprocket / teeth of front sprocket*. But for historical reasons in cycling it is common to use the inverse ratio [Gre05].

As a matter of simplicity, for the moment further stages of gearing within an ergometer are ignored.

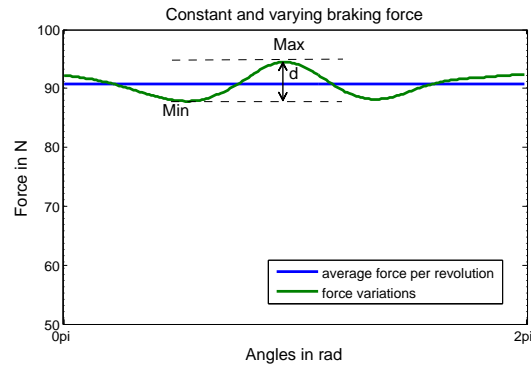


Figure 2.6: The green line denotes the braking force varying due to the angular velocity, whereas the blue line shows the constant force if assumed that velocity variations are adjusted by changing the supplied current. The difference between the minimum (Min) and the maximum (Max) of the varying braking force is denoted  $d$ .

The SRM ergometer computes power based on the mean force applied to the pedal and the mean angular velocity of the crank during a pedal cycle. The ergometer was set to a fixed power level, which is assured by automatically adapting the resistance of the eddy current brake based on the actual power measurements.

Since power and cadence were claimed to be kept constant, the course of the resistance provided by the eddy current brake is expected to be rather constant as well. Actually, the resulting power measurements were not that constant. This is a further indicator for a constant braking resistance, as a quickly changing braking resistance should have been able to enforce a more constant power level.

Thus, the braking force is assumed to resemble this average force, which can be retrieved from power and cadence data delivered by the SRM ergometer.

The torque provided by the eddy current brake is proportional to the angular velocity of the flywheel. Therefore, variations of angular velocity within a pedal circle will cause variations of braking force, if the current supplied remains constant. As it is not clear if the brake automatically adjusts the current to diminish fluctuations caused by the within pedal cycle variations of angular velocity, the resulting braking forces of both cases shall be examined.

If the eddy current brake does not adjust the current with respect to the variations of the angular velocity within a pedal cycle, the braking force variations would be proportional to those of the angular velocity of the flywheel. Thus, when regarding the braking force transferred to the pedal, these variations would be proportional to the angular velocity of the crank.

The varying braking force was determined by means of the average power per pedal cycle and the angular velocity of the crank, whereas the constant braking force was determined using the average per pedal cycle velocity of the crank instead. A resulting braking force profile is exemplarily shown in Figure 2.6.

The difference  $d$  between the minimal and maximal variation of the force per pedal cycle amounts to about 9 % of the average force per pedal cycle (in average over all accomplished measurements). As mentioned before, it might be the case that the eddy current brake automatically adjusts the current to reduce these fluctuations. Otherwise, oscillating variations of the braking force (Figure 2.6) occur, but with respect to the absolute value of the force those deviations are relatively small.

## 3 Data Acquisition

The practical experiments took place at the Radlabor Freiburg (Radlabor GmbH, Freiburg, Germany). They were conducted indoors on an SRM Ergometer. By means of a LUKOtronic motion capture system the pedal movement was recorded. Furthermore, power and cadence were measured using a SRM training system. A later evaluation of the quality of the computed pedal force demands a reference value. For this purpose the pedal force was captured with the Powertec System [SMO<sup>+</sup>07].

The measuring instruments are shortly introduced in Section 3.1. Afterwards the experimental setup (Section 3.2) and the series of measurement (Section 3.3) are described.

### 3.1 Measuring Instruments

This Section outlines the operation principles of the measuring instruments used in this thesis. Those are the LUKOtronic Motion Capture System (Section 3.1.1), the SRM Ergometer (Section 3.1.2), the SRM Training System (Section 3.1.3) and the Powertec System (Section 3.1.4).

#### 3.1.1 LUKOtronic Motion Capture System

Before considering the LUKOtronic Motion Capture System some fundamentals regarding motion capturing in general are covered.

##### Motion Capturing

Motion data are three dimensional coordinates of points of a moving object. Those points might correspond to joints of a human being, as well as the pedal of a bicycle. The coordinates are measured at very short intervals, for example at several hundreds Hz. Thus, motion is captured as a sequence of three dimensional coordinates of individual points.

For the measurement of motion data mainly mechanical, magnetic, or optical systems are used. A short introduction to motion capturing offers amongst others [Ger04] and a detailed overview is given in [Men00].

Optical motion capture systems consist of at least two CCD (charge-coupled device) cameras which contain a matrix of photoelectric cells to track the motion of markers attached to the moving object. The markers are either passive,

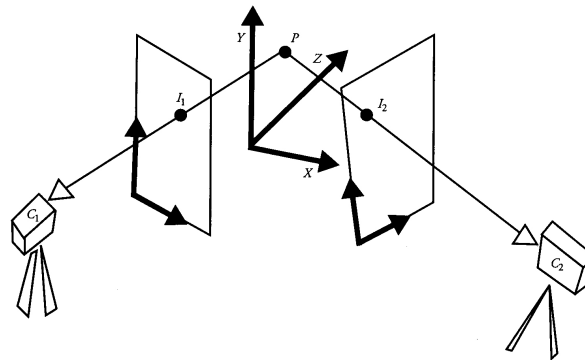


Figure 3.1: Rays from marker with real world position  $P$  to the camera centres are projecting the marker to image coordinates  $I_1$  and  $I_2$ . Source: [Par02, p. 374].

which means they reflect light, or they actively emit infrared light.

The real world three-dimensional position of a marker maps to a position of the two-dimensional image plane of the camera, which is illustrated in Figure 3.1. The reconstruction of the world position then is based on the fact that it must be somewhere on the straight line passing from the camera centre (i.e., the centre of projection) through the image coordinates. When two cameras are used, each defines such a straight line corresponding to the same marker position. In the absence of noise, these two lines would intersect at the real world position of the marker (as shown in Figure 3.1). In reality, measurements are not totally accurate and hence the two lines generally do not intersect. Thus, the marker position has to be estimated by least squares methods.

The reconstruction of markers includes further steps, as for example camera calibration, and is far more complex as outlined here. For an in-depth view on this topic see [HZ04].

### LUKOtronic Analysis System AS 200

Motion capture in the course of this thesis was carried out using the LUKOtronic Analysis System AS 200 (LUKOtronic company), see Figure 3.2. This optical motion capture system uses active infrared markers in combination with a measurement bar consisting of three infrared cameras.

The highest frame rate possible by the LUKOtronic system is about 1200 Hz divided by the number of markers used. The LUKOtronic website reports a local resolution of the camera of  $15 \mu\text{m}$  and an accuracy of 2 mm. On the other hand, the system description accompanying the LUKOtronic system states a resolution of 0.1 mm at a distance of 1.5 m. No details about the reconstruction of the real world marker positions is revealed in the system description.



Figure 3.2: Camera and markers of LUKOtronic System

### 3.1.2 SRM Ergometer

The main features of the SRM High Performance Ergometer (see Figure 3.4(a)) are the different riding modes and the large flywheels. A detailed description is found in the according handbook [Woo06]. The SRM Ergometer includes a SRM Training System, which is described in the next Section.

The three riding modes are *hyperbolic*, *isokinetic* and *open ended*. Corresponding selections are defined by the user by means of the software. In hyperbolic mode (which was used for the experiments), the required power output has to be specified. Depending on the actual measured power while riding, the resistance of the eddy current brake is adapted to provide the desired power.

In isokinetic mode a constant cadence is ensured regardless of the crank position or the power output. Therefore, the angular velocity of the brake is controlled and its resistance is adapted to prevent pedalling above the chosen cadence (but pedalling below is possible).

In open ended mode, the resistance of the brake increases proportionally to the speed to imitate rolling resistance on the road. The cyclist can freely choose and alter cadence and resistance during the session.

The use of the different flywheels and shifting gears in the internal hub in combination with the chosen cadence provides a variety of kinetic energy profiles from about 60 J up to 14050 J. Tables regarding the choice of appropriate profiles based on mass of cyclist and riding speed can be found in the manual [Woo06]. This allows an authentic simulation of riding on the road.

### 3.1.3 SRM Training System

The SRM training system (see Figure 3.3) is a performance measuring device which is acknowledged to be the "Gold Standard" for power measurement [Woo07]. It is widely-used by professional cyclists and also by amateurs. For a detailed description it is referred to the user manual [Woo07]. The SRM Training System consists of the PowerMeter and the PowerControl.

The PowerMeter is composed of the crank, chainrings, and the measuring unit that is placed between crank and chainrings. The force applied to the pedals is determined by measuring the voltage of strain gauge strips inside of the PowerMeter. By the exertion of force on the crank, the strain gauges deflect

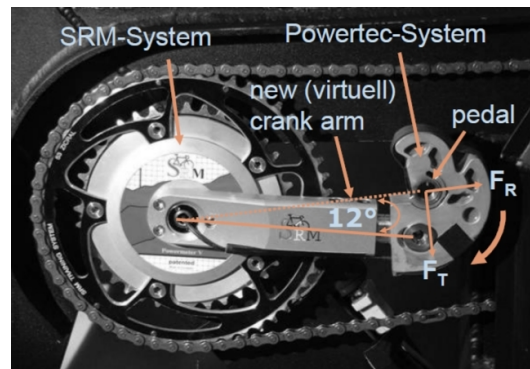


Figure 3.3: Powertec System mounted on SRM Training System. Source: [http://www.radlabor.de/fileadmin/Radlabor/03\\_produkte/Shop\\_\\_\\_Messsystem/Radlabor\\_Powerforce-System\\_incl.\\_price.pdf](http://www.radlabor.de/fileadmin/Radlabor/03_produkte/Shop___Messsystem/Radlabor_Powerforce-System_incl._price.pdf)

and in consequence their resistance alters. Thus, also the voltage changes accordingly and likewise the measured torque, which is based on this voltage. The cadence is measured by means of a reed switch within the PowerMeter that releases a pulse once per crank revolution.

Torque and cadence are transmitted to the PowerControl, which is a bicycle computer attached to the handlebars. It is able to provide information about power, cadence, velocity, and heart rate. Power is calculated by multiplying average torque per respective revolution and according cadence. The torque data itself is not made available to the user.

There exist several types of SRM Training Systems. For the experiments performed within this thesis a scientific version was used. It includes eight strain gauges and its accuracy is  $\pm 0.5\%$ .

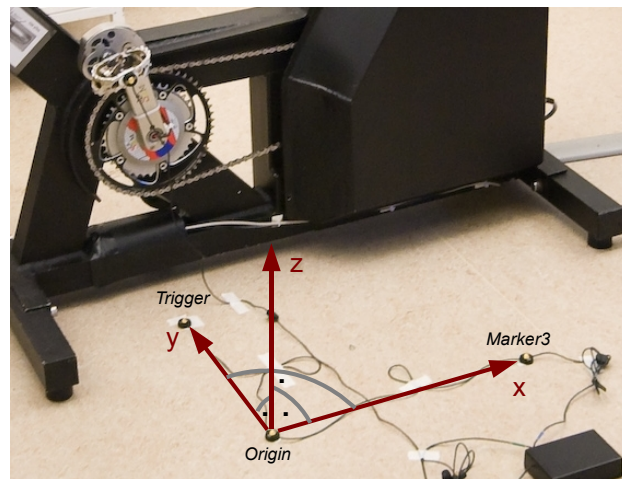
### 3.1.4 Powertec

The Powertec System [SMO<sup>+</sup>07] measures tangential and radial forces separately for the left and the right foot. It is mounted between the crank and the pedal, and it can be attached to every type of crank and used with arbitrary pedals. Figure 3.3 shows the Powertec System in large. It can be seen mounted next to the pedal in Figure 3.4(b).

The force is determined by the use of two Hall effect sensor systems. When applying a force a sensor is displaced, and this in turn causes a change in the magnetic field. The force can be decoupled into the tangential and the radial part (with respect to the crank) as the two sensors are located orthogonal to each other and in direction of those two forces.



(a)



(b)

Figure 3.4: Setup of measuring instruments (a), and coordinate system as defined by motion capturing system (b).

## 3.2 Experimental Setup

For the measurements, an SRM Ergometer (comprising the SRM Training System) was used with the Powertec System attached between cranks and pedals (see Figure 3.4(a)). The LUKOtronic measurement bar is located in parallel to the right side of the ergometer at a distance of about 1.6 m.

Four infrared markers were used. One was fixed onto the pedal axis, another one (in the following named *Trigger*) perpendicular underneath the crank on the floor to identify the beginning of each pedal revolution. Two more markers (referred to as *Origin* and *Marker3*) were fixed on the floor to define a coordinate system, together with the other marker on the floor (see Figure 3.4(b)). The chosen sampling rate of 295 Hz was the highest possible.

### 3.3 Series of Measurements

Four persons participated in the experiments. Two of them (subject B and C) used clipless pedals, while both other subjects (A and D) used normal platform pedals with ordinary sports shoes.

The measurement consisted of two main series that differed in cadence. For the first series, the probands were asked to maintain a low cadence of about 80 rpm, and during the second series a high cadence of approximately 120 rpm was demanded.

During both measurement series the SRM Ergometer was set to constant power mode, which means pedalling at the predetermined power was ensured by the ergometer (see also Section 3.1.2). Measurements of both series were taken at the same specified power settings. Each series started with a power level of 100 W, and the power levels were increased by 100 W for each new level. A power level had to be hold for one minute. Between two power levels the riders were instructed to pedal two minutes at 50 W to recover.

The maximum power level was individually dependent on force and condition of the single proband. This resulted in proband A and D reaching level 100 W, 200 W and 300 W. Proband B additionally managed 400 W and proband C even 500 W. The settings in order of the execution of the measurements are shown in Table 3.1.

---

No.	Person	Cadence in rpm	Power in Watt
1	A	80	100
2	A	80	200
3	A	80	300
4	B	80	100
5	B	80	200
6	B	80	300
7	B	80	400
8	A	120	100
9	A	120	200
10	A	120	300
11	B	120	100
12	B	120	200
13	B	120	300
14	B	120	400
15	C	80	100
16	C	80	200
17	C	80	300
18	C	80	400
19	C	80	500
20	C	120	100
21	C	120	200
22	C	120	300
23	C	120	400
24	C	120	500
25	D	80	100
26	D	80	200
27	D	80	300
28	D	120	100
29	D	120	200
30	D	120	300

Table 3.1: Measurements in chronological order of execution.

## 4 Pedal Force Computation

This thesis is restricted to the computation of the tangential (effective) component of the pedal force that was revealed to be the most important one regarding the improvement of cycling performance (see Section 2.1). The aim is to determine pedal force using the angular acceleration of the crank by capturing its motion. Since this motion is caused solely by the crank torque (which is due to the tangential force), the radial component cannot be gathered following this approach.

It is desirable to measure the tangential pedal force of the left and the right foot separately. For example, this allows to uncover asymmetries of the pedalling behaviour between the two legs.

Nonetheless, knowing only the total tangential force (i.e., the sum of the tangential pedal force of the left and right foot) still permits the perception of asymmetries [BG96]. However, it cannot be identified which foot applied more or less force than the other, whether during upstroke or downstroke. Figure 2.3 visualises both cases.<sup>1</sup>

The measurement procedure chosen in this thesis is based on the motion of the crank, which is caused by both feet simultaneously. Hence, it is not possible to determine which fraction of the motion is caused by which foot. Consequently, the tangential force can only be uncovered as the sum of the left and right foot together. Unless explicitly stated otherwise, in the following the term *pedal force* always denotes the total tangential force applied to the left and the right pedal.

Based on the considerations in Section 2.2.2, an attempt is made to determine pedal force  $F_P$  by means of the force  $F'_B$  opposed to braking force and  $F'_I$  opposed to inertial force :

$$F_P = F'_B + F'_I . \quad (4.1)$$

The essential computations are depicted in Figure 4.1. The left branch of the diagram (i.e.,  $F'_B$ ) is dealt with in Section 4.1. Subsequently, Section 4.2 considers the right branch (i.e.,  $F'_I$ ).

In Section 4.3 the computation of the total tangential force by means of the Powertec System is depicted, which will be used as the reference value in Chapter 6.

Due to different sampling frequencies of the SRM Training System, the LUKOtronic System, and the Powertec System, the data has to be interpolated.

---

<sup>1</sup>Actually, the figure shows torque profiles, but the shape of the curves is the same for the corresponding force profiles.

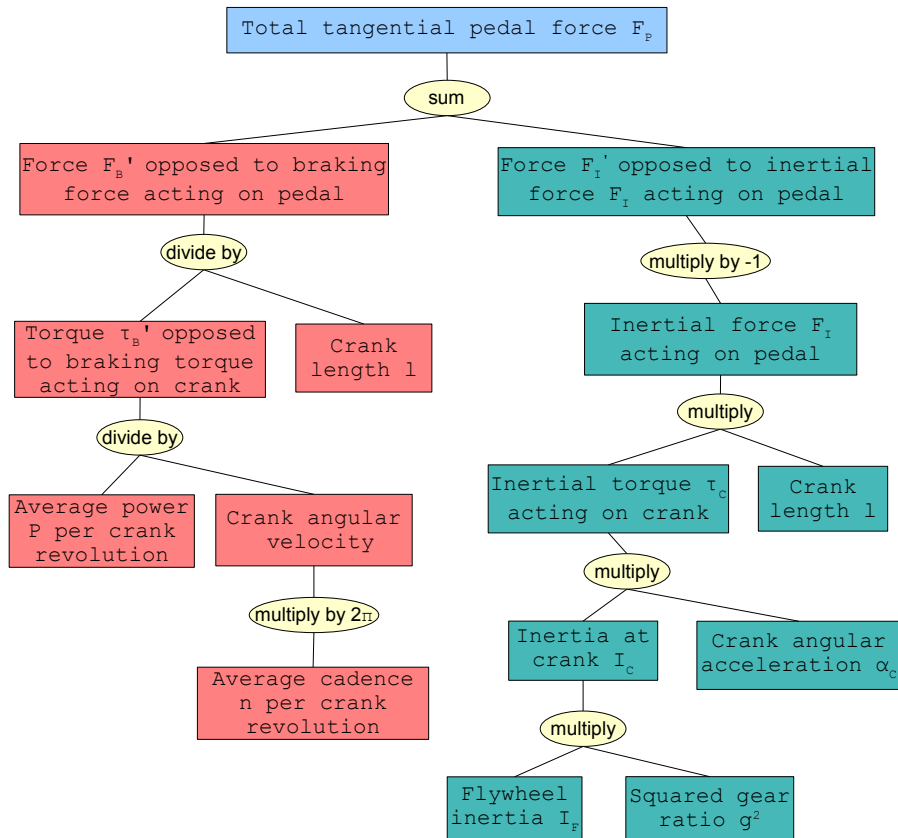


Figure 4.1: Outline of pedal force computation.

Further it has to be synchronised. These issues are covered in Section 4.4.

## 4.1 Braking Force

The SRM System determines power with a frequency of 2 Hz by means of average crank torque and average cadence during a crank revolution. As discussed in Section 2.2.3, the according pedal force is assumed to correspond to the resistive force of the brake.

Since the pedal force data captured by the SRM System is not made available to the user but cleared after the power computation, it has to be recovered using the power and cadence data.

Let  $F'_B$  denote the proportion of the force exerted onto the pedal which is due to the braking force  $F_B$ . This means  $F'_B$  has the same magnitude as  $F_B$  but the opposite direction. Force  $F'_B$  can be obtained from the average torque around the crank axis  $\tau'_B$  and the crank length  $l$ :

$$F'_B = \frac{\tau'_B}{l}, \quad (4.2)$$

where in this case  $l = 0.175$  m. In turn, the torque  $\tau'_B$  depends on the power  $P$  applied to the pedals and the angular speed  $\omega_C$  of the crank by

$$\tau'_B = \frac{P}{\omega_C} . \quad (4.3)$$

The angular speed  $\omega_C$  (unit rad/s) can be computed from cadence  $n$  (unit rpm) by a unit transformation:

$$\omega_C = 2\pi \cdot n . \quad (4.4)$$

Using (4.2), (4.3), and (4.4), force  $F'_B$  is gained by

$$F'_B = \frac{P}{2\pi \cdot n \cdot l} . \quad (4.5)$$

Assuming that the SRM measurements correspond to force  $F'_B$ , this force is retrieved by insertion of SRM power and cadence data into (4.5).

## 4.2 Inertial Force

The inertial force is caused by the inertia of the rotating flywheel contained in the cycling ergometer, which is driven by pedalling.

The resistive torque  $\tau_{F,I}$  about the axis of rotation of the flywheel is due to the flywheels moment of inertia  $I_{F,I}$  and its angular acceleration  $\alpha_F$ :

$$\tau_{F,I} = I_{F,I} \cdot \alpha_F . \quad (4.6)$$

In the same way, the resultant inertial torque at the crank  $\tau_{C,I}$  can be determined by the moment of inertia of the flywheel transferred to the crank  $I_{C,I}$  and the angular acceleration of the crank  $\alpha_C$ :

$$\tau_{C,I} = I_{C,I} \cdot \alpha_C . \quad (4.7)$$

The inertia transferred to the crank  $I_{C,I}$  follows from

$$I_{C,I} = I_{F,I} \cdot g^2 , \quad (4.8)$$

where  $g$  denotes the gear ratio.

The torque  $\tau_{C,I}$  at the crank can be determined using (4.7), and (4.4) and it follows for the inertial force  $F_{C,I}$  opposed to the motion of the pedal:

$$F_{C,I} = \frac{\tau_{C,I}}{l} = \frac{I_{F,I} \cdot g^2 \cdot \alpha_C}{l} . \quad (4.9)$$

Hence, the proportion  $F'_{C,I}$  of the total pedal force which is needed to overcome the inertial force  $F_{C,I}$  is obtained by

$$F'_{C,I} = -F_{C,I} , \quad (4.10)$$

which means it has the same magnitude as  $F_{C,I}$  but in opposite direction.

Obviously, to obtain the inertial force  $F_{C,I}$  two constants (the flywheel moment of inertia  $I_{F,I}$  and the gear ratio  $g$ ) and the crank angular acceleration  $\omega_C$  have to be determined. As the estimation of the angular acceleration is a complex task, it is dealt with separately in Chapter 5.

### Flywheel moment of inertia

The SRM Ergometer comes with two different flywheels with the shape of a disk. Both, one of them, or neither can be mounted. For the experiments the small flywheel was used. Its moment of inertia  $I_F$  is determined by

$$I_F = \frac{1}{2}mr^2,$$

where  $m$  denotes the mass and  $r$  the radius of the flywheel. Corresponding to [EJG<sup>+</sup>07] the mass of the small flywheel is 4.612 kg and its radius is 0.125 m. Hence, the flywheel moment of inertia is 0.036 kgm<sup>2</sup>.

This value does not account for other moving parts of the ergometer (as for example the cranks). Their moment of inertia is assumed to be relatively small [EJG<sup>+</sup>07] and is neglected subsequently.

### Gear ratio

The total gear ratio  $g$  of the SRM ergometer is the product of the crankset gear ratio, two fixed stages of gearing, and the internal Rohloff hub gear ratio. During the measurements the internal gear ratio and the number of teeth of the rear sprocket were not checked. Instead the gear ratio had to be determined afterwards based on the captured cadence and speed measurements of the SRM ergometer. The formula which is internally used to compute speed  $s$  based on gear ratio  $g$ , cadence  $n$ , and circumference  $c$  of the rear wheel was obtained from SRM. This equation is resolved to provide the gear ratio:

$$g = \frac{s}{n \cdot c \cdot f_1 \cdot f_2}, \quad (4.11)$$

where  $c$  has to be set to 1 m with respect to the non-existing rear wheel when using the SRM Ergometer. The factors  $f_1$  and  $f_2$  are used for the conversion from cadence to speed.<sup>2</sup> The resulting gear ratio  $g$  is  $\approx 14.4706$ .

<sup>2</sup>The values of the two factors are  $f_1 = 0.006$  and  $f_2 = 4$ . According to SRM,  $f_1$  is used to convert measured revolutions per minute to speed. Revolutions per minute are measured 4 times per revolution. Thus, when using displayed cadence instead of the measured revolutions, cadence has to be multiplied by 4.

### 4.3 Powertec Pedal Force

The Powertec Systems measures tangential and radial pedal force separately for the left and the right foot. Hence, for the computation of the total tangential force, the tangential force data for the left and right foot simply need to be added.

During measurements the Powertec Systems uses a trigger to indicate each point in time when the left pedal reaches the top death centre of the pedal cycle. This trigger is used to define the beginning or end of each crank revolution.

The average force per cycle (i.e., the sum of measured force values per cycle divided by their number) is also determined, as it is needed for synchronisation purposes in Section 4.4.

### 4.4 Synchronisation

The computation of the pedal force and its evaluation in reference to the Powertec force require interpolation and synchronisation of the LUKOtronic, SRM, and Powertec measurement data.

Since pedal force shall be determined with high angular resolution, motion capturing was accomplished with the highest possible frame rate, which is 295 Hz. The sampling rate of the Powertec System is 1000 Hz and that of the SRM System is 2 Hz. Therefore, both SRM and Powertec data is interpolated at 295 Hz. For the SRM data piecewise cubic Hermite interpolation and for the Powertec data linear interpolation was used.

The Powertec and LUKOtronic System were synchronised manually. By means of the triggers, both systems specify the same moments in time, when the left pedal is at the top death centre (Powertec) and the right pedal is at the bottom death centre (LUKOtronic). Hence, for each measurement the devices were started by hand at approximately the same time. Then, data prior to the first trigger, which is before the start of the first complete revolution, was removed.

The SRM system kept running throughout each whole series per person, such that for each subject one data set exists for all power levels (including rest periods) with a cadence of 80 rpm and one for all power levels with 120 rpm. Therefore, these data sets are divided into approximate fragments containing a single power level.

The exact synchronisation of the SRM data with the motion data was based on the cross-covariance between the cadence measured by SRM and cadence

determined by means of the motion data.<sup>3</sup> The lag value with the largest cross-covariance was used to define the Section of the SRM file corresponding to the LUKOtronic measurement.

The same method is used to synchronise SRM and Powertec measurements. This time, it is based on the force which can be determined by SRM power and cadence, and the average force computed for the Powertec data. Synchronising SRM with LUKOtronic and Powertec both yielded the same fragments of the SRM measurements. Hence, LUKOtronic and Powertec are assured to be properly synchronised as well.

---

<sup>3</sup>The cross-covariance sequence  $c_{xy}$  of the sequences  $x$  and  $y$  is estimated using MATLAB function `xcov` as the sequence

$$c_{xy}(m) = \begin{cases} \sum_{n=0}^{N-|m|-1} \left( x_{n+m} - \frac{1}{N} \sum_{i=0}^{N-1} x_i \right) \left( y_n^* - \sum_{i=0}^{N-1} y_i^* \right) & m \geq 0 \\ c_{xy}^*(-m) & m < 0 \end{cases}$$

of length  $N$ .

The motion data based cadence  $n$  follows from the average angular velocity per revolution  $\omega_{avg}$  by  $n = \frac{\omega_{avg}}{2\pi}$ .

# 5 Crank Angular Acceleration

In the last chapter the computation of pedal force was described, omitting the actual estimation of the crank angular acceleration. The proper identification of this acceleration is a challenging task as the motion capture data is affected by different sources of errors as discussed in Section 5.1.

Prior to the derivative estimation some preprocessing is carried out (Section 5.2). This includes a transformation of the three-dimensional into two-dimensional data.

In Section 5.3, the noisy data is filtered by means of a Butterworth Filter, a Kalman Smoother, and Singular Spectrum Analysis. Finally, in Section 5.4 the computation of derivatives is described.

## 5.1 Problems Affecting Derivative Estimation

Measurement noise caused by the accuracy and resolution of the cameras is a serious problem when estimating derivatives, as outlined in the introduction. The characteristics of the measurement noise affecting the accomplished measurements is analysed in Section 5.1.1.

The second problem regarding the motion data could rather be denoted as an instrumental error. The angular acceleration of the crank is defined by the pedal axis movement on a circle around the bottom bracket. It turned out that the pedal marker trajectory was not moving on an almost perfect cycle but rather ellipsoidal. This is further discussed in Section 5.1.2.

### 5.1.1 Measurement Noise

When filtering or smoothing noisy measurements it is useful to analyse certain aspects of the noise. Many filtering and smoothing methods require the noise to be white and zero mean Gaussian to yield optimal results. Henceforth, the underlying noise of the motion measurements shall be tested for Gaussian distribution with zero mean in Section 5.1.1.2 and for whiteness in Section 5.1.1.3. The variance of noise that is also needed especially for Kalman Filtering is determined in Section 5.1.1.4. Preceding, the identification of the noise itself is discussed in Section 5.1.1.1.

The main problem regarding the analysis of noise is that usually no measurement of noise separated from the actual motion data exists. The measurement of the moving pedal cannot simply be divided into noise and a noise-free

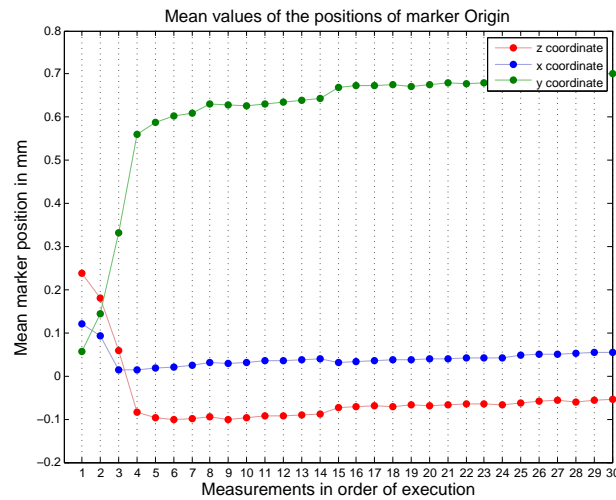


Figure 5.1: Variation of the mean value in course of the measurements. (For the details of each measurement refer to Table 3.1.)

measurement. Thus, not the noise of the pedal marker will be analysed, but that of the markers on the floor.

Those markers fixed on the ground for the definition of the coordinate system should not move during the course of the measurements. Therefore, the variations of their measurements (i.e., the actual measured positions minus the mean position) are regarded as noise.

The accuracy of the motion capture system is sometimes not the same for all directions [Cha08]. Regarding the LUKOtronic system, corresponding information is not available to the author. Due to different spatial positions of the markers, their distances and angles to the cameras are not the same. Hence, the accuracy of the measurement of the markers might differ as well.

### 5.1.1.1 Floor Markers

The three markers on the floor are arranged as shown in Figure 3.4(b) and are labelled *Origin*, *Marker3*, and *Trigger*. Since their behaviour differs, they are analysed individually.

First an aspect is discussed which concerns the three markers in the same way. As mentioned before, the floor markers were fixed on the ground and their mean position should not change. However, their positions slightly changed during measuring. Figure 5.1 exemplarily shows the mean values of the position of marker *Origin* in the course of the different measurements. The positions of the other two floor markers are changed in the same way.

In retrospect, the cause for this movement cannot be identified reliably. The main change of position between measurements 3 and 4 might be due to a restart of the LUKOtronic software, which causes a recalibration of the cameras.

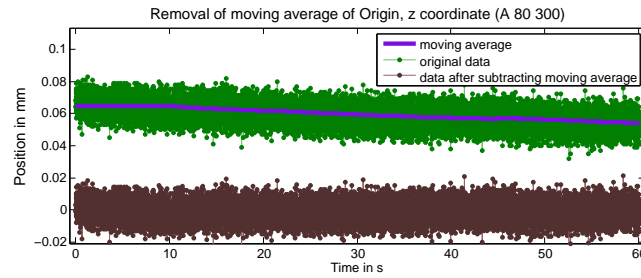


Figure 5.2: The movement of an exemplary floor marker is visualised. The measured data, the moving average and data after subtraction of the moving average are shown.

It is also possible that someone touched the camera unintended and unnoticed. A movement of the measurement bar while the system is used causes the measurement data to become incorrect [LUK]. Maybe the slight movements starting from measurement 4 are due to such incorrectness. Also infrared light influencing the measurements could be a possible reason, even though attendants were asked to deactivate sources of infrared (as for example in mobile phones). The lightning conditions (changing daylight, switching on/of artificial light) could be a reason as well.

Due to that minimal movement it is not appropriate to simply subtract the mean from the positions data for the separation of position data and noise. This problem was dealt with by using an moving average instead of the mean. To ensure that the moving average follows the changing position of the marker, but not the slight variations due to actual noise, a window size of 3000 for the moving average is chosen (the sample size per measurement is about 18000). In the following, the motion data after subtraction of the moving average will be considered as the noise of the floor markers. Figure 5.2 exemplarily shows the measurement itself, the moving average, and the resulting noise.

### Marker *Marker3*

*Marker3* does not exhibit irregularities during the first three measurements (see Figure 5.3(a)). Starting from measurement 4, the  $x$ - and  $y$ -coordinate are affected by a big amount of outliers pointing in one direction, as shown in Figure 5.3(b). The  $z$ -coordinate does not show this behaviour, but its values vary over a broader range. The outliers are smaller than the accuracy of the LUKOtronic System denoted as 2 mm. Hence, this effect might be caused by the real world marker reconstruction based on the image coordinates. Since technical details of the LUKOtronic System and the reconstruction methods are not available to the author, that cannot be clearly resolved.

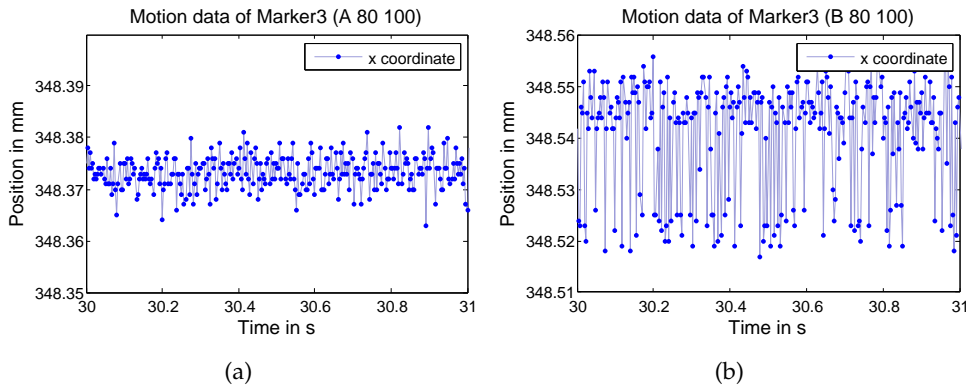


Figure 5.3: (a) exemplarily presents the measurement of *Marker3* of the first three measurements, whilst (b) demonstrates the corruption of the following measurements.

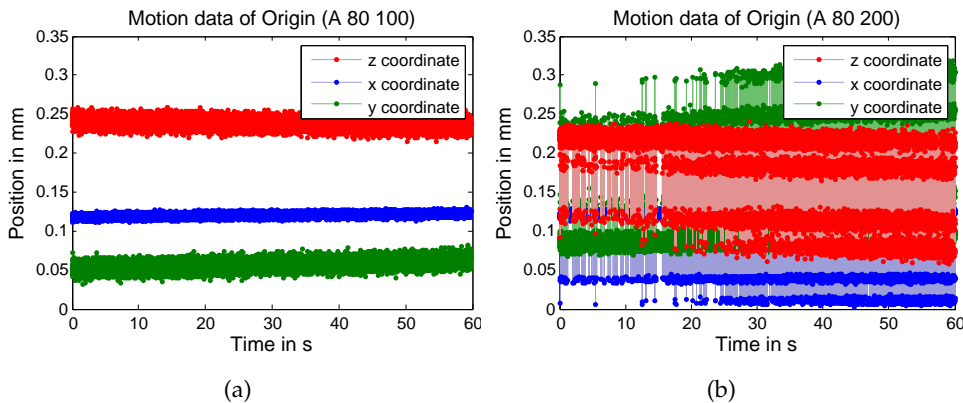


Figure 5.4: (a) shows the first measurement of marker *Origin*, (b) the second, which is highly corrupted.

### Marker *Origin*

The measurement data of marker *Origin* does not contain abnormalities except for the second recording. Figure 5.4(b) shows the distortion of measurement 2, whereas all other measurements resemble Figure 5.4(a).

### Marker *Trigger*

Throughout all measurements, the data of marker *Trigger* is infiltrated by outliers in both directions which are not assumed to be caused by measurement inaccuracies (see Figure 5.5).

The marker *Trigger* was fixed with sticky tape on the floor underneath the pedal. Thus, a possible explanation of these outliers might be the marker chain of the pedal marker touching that of marker *Trigger* while pedalling. Therefore, the angular crank positions according to the occurrences of the outliers

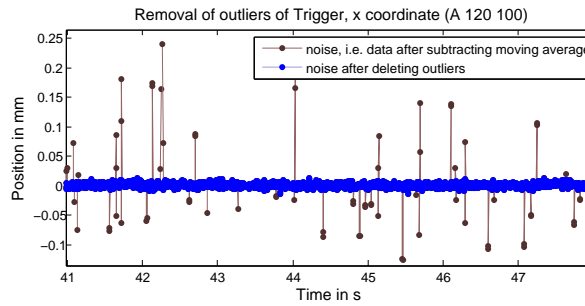


Figure 5.5: Noise of marker *Trigger* before and after removal of outliers.

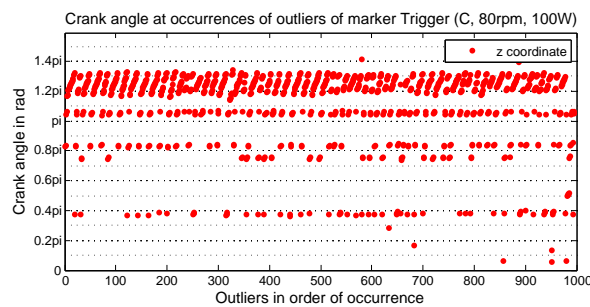


Figure 5.6: The angular position of the crank during the occurrences of outliers.

are analysed. Figure 5.6 shows that the occurrence of the outliers is highly correlated with the angular position of the crank. This supports the assumption that the outliers are due to a slight motion caused by the marker chains.

Thus, the outliers are not interpreted as noise. They are excluded from further analysis of the floor marker noise, which means they are removed from the measurement data before examining Gaussian distribution, whiteness, and variance. Anyhow, the removal of potential outliers might still miss to recognise some of them and wrongly identify others.

By having a close look at the measurement data, the outliers are defined as measurement values more than a certain distance apart from the moving average. For the  $x$ -coordinate, the chosen distance is 0.015 mm, for the  $y$ -coordinate 0.05 mm, and for the  $z$ -coordinate 0.04 mm. The noise of *Trigger* before and after a deletion of these outliers is exemplified in Figure 5.5.

### 5.1.1.2 Gaussian Distribution

A Gaussian distribution of data can be identified using formal normality tests or graphically by comparing a histogram of the data to a normal probability curve. Both procedures are error-prone.

### Formal Normality Tests

For normality testing the *Jarque Bera*, *Lilliefors*,  $\chi^2$  goodness-of-fit, and the *Shapiro-Wilk / Shapiro-Francia* test are used.<sup>1</sup> The null hypothesis is a normal distribution of the data, the alternative hypothesis stands for non-normality. A 5% significance level is chosen.

As the present sample size is very large ( $\approx 18,000$  samples per recording), normality tests usually tend towards refusing normality. The confidence intervals are narrowed and the tests become too powerful. This means they are very sensitive to even minor deviations from normality, which occur in every real data set. Table 5.1(a) shows the test results for all floor markers and all measurements. In almost all cases the normality assumption is rejected.

Conducting the tests only based on a smaller section of the data (100 samples) yields quite different results, as presented in Table 5.1(b). This time normality is rejected only for those cases in which the marker behaviour was corrupted.

As described in Section 5.1.1.1, the  $x$ - and  $y$ -coordinates of the noise of *Marker3* contain many outliers pointing in one direction. And for these two coordinates, the normality test reveals non-normality but not for the  $z$ -coordinate. Marker *Origin* was very noisy during measurement 2 and all tests reject normality for these measurements. During the remaining measurements marker *Origin* did not show major irregularities, and the normality test indicate a normal distribution in most cases for the  $y$ - and  $z$ -coordinates and in more than half of the tests for the  $x$ -coordinate. Also, for marker *Trigger* after outlier removal the tests mostly hold the normality hypothesis.

### Comparison of Histogram to Normal Probability Curve

To determine visually how well the data fits a normal distribution, histograms of the data together with the estimated normal curves are plotted. This method gives a good idea about the distribution. Nevertheless, it might lead to wrong conclusions, as the shape of the histogram strongly depends on the number of bins used for the histograms and their positions.

Histograms (consisting of 50 bins) of the floor marker noise were plotted and compared with corresponding estimated normal probability curves. The observations are in accordance to those of the formal tests over a subsequence of 100 samples. Figure 5.7 shows representative examples of the histograms for marker *Origin*, *Marker3* and *Trigger* respectively.

<sup>1</sup>For the Jarque Bera, Lilliefors, and  $\chi^2$  goodness-of-fit test the MATLAB Statistics Toolbox functions `jbttest`, `lillietest` and `chi2gof` were used (refer to the MATLAB documentation, online: <http://www.mathworks.de/access/helpdesk/help/toolbox/stats/> [Accessed 14.02.2009]). The Shapiro-Wilk / Shapiro-Francia normality tests was conducted using Ahmed Ben Saïda's MATLAB implementation `swtest.m` (Online: <http://www.mathworks.com/matlabcentral/fileexchange/13964> [Accessed 10.02.2009]). Depending on the kurtosis of the data, the function executes a Shapiro-Wilk or a Shapiro-Francia test.

(a)

Measurement no.	Marker3			Origin			Trigger		
	x	y	z	x	y	z	x	y	z
	JLCS	JLCS	JLCS	JLCS	JLCS	JLCS	JLCS	JLCS	JLCS
1	1111	1111	1011	0111	0100	1111	1111	1111	1111
2	1111	1111	1011	1111	1111	1111	1111	1111	1111
3	1111	1111	0000	0111	0110	1111	1111	1111	1111
4	1111	1111	1111	0111	0101	0101	1111	1111	1111
5	1111	1111	1111	1111	1111	0101	1111	0111	1111
6	1111	1111	1111	0111	1111	0111	1111	0111	1111
7	1111	1111	1111	1111	1111	0111	1111	1001	1111
8	1111	1111	1111	1111	0111	1111	1111	1111	1111
9	1111	1111	1111	0111	0100	1111	1111	1111	1111
10	1111	1111	1111	0111	0101	1111	1111	1111	1111
11	1111	1111	1111	1111	0111	1111	1111	1111	1111
12	1111	1111	1111	1111	0101	1111	1111	1111	1111
13	1111	1111	1111	1111	0111	1111	1111	1011	1111
14	1111	1111	1111	1111	1111	1111	1111	0001	1111
15	1111	1111	1111	0101	1101	1111	0111	1111	1111
16	1111	1111	1111	0111	1101	1111	1111	0111	0111
17	1111	1111	1111	0101	0101	1111	1111	1111	1101
18	1111	1111	1111	0101	0100	1111	1111	1111	0000
19	1111	1111	1111	0111	1111	1111	1111	1111	0000
20	1111	1111	1111	1111	1101	1111	1111	1111	1111
21	1111	1111	1111	1101	0111	1111	1111	1111	0111
22	1111	1111	1111	1111	0100	1111	1111	1111	0011
23	1111	1111	1111	0111	0100	1111	1111	1111	0111
24	1111	1111	1111	0111	1111	1111	0111	1111	0111
25	1111	1111	1111	0111	0100	1111	1111	1111	1111
26	1111	1111	1111	1111	1101	1111	1111	1111	1111
27	1111	1111	1111	1111	0100	1111	1111	1111	1111
28	1111	1111	1111	1111	0100	1111	1111	1111	1111
29	1111	1111	1111	1111	0101	1111	1111	1111	1111
30	1111	1111	1111	1111	0111	0111	1111	1111	1111

(b)

Measurement no.	Marker3			Origin			Trigger		
	x	y	z	x	y	z	x	y	z
No.	JLCS	JLCS	JLCS	JLCS	JLCS	JLCS	JLCS	JLCS	JLCS
1	0000	0100	0000	0100	0000	0001	0101	0000	0000
2	0110	0000	0000	1111	1111	1111	1111	0001	0000
3	0111	1000	0110	0101	0010	0000	0101	0000	0110
4	1111	0101	0010	0100	0000	0000	0010	0000	0000
5	1111	1111	0000	0110	0000	0000	0111	0000	0000
6	1111	1111	0000	0100	1101	0000	0101	0000	0000
7	1111	1111	0000	0101	0000	0000	1101	1001	1001
8	1111	1111	0000	0101	0000	0110	0000	1111	0000
9	1111	1111	1111	0000	0010	0000	0110	0000	0000
10	1111	1111	0000	0110	0000	0000	0000	1000	0000
11	1111	1111	0011	0100	0000	0000	0000	0000	0010
12	1111	1111	0000	0101	0000	0000	0000	0000	1111
13	1111	1111	0101	0100	0000	0000	0100	0000	0010
14	1111	1111	0000	0111	0000	0000	0101	0000	0100
15	1111	1111	0000	0101	0000	0000	0000	0100	0000
16	1111	1111	0000	0111	0000	0000	0000	0000	0000
17	1111	1111	1001	0111	0000	0000	0000	1000	0000
18	1111	1111	0000	0101	1111	0000	0100	0000	0000
19	1111	1111	0011	0100	0000	0110	0100	0100	0000
20	1111	1111	0100	0101	0100	0000	0000	0000	0010
21	1111	1111	0000	0101	0000	0000	0111	1111	0000
22	1111	1111	1001	0110	0100	0110	0000	0000	0001
23	1111	1111	0010	0101	0010	0010	0100	0000	0101
24	1111	1111	0000	0111	0000	0000	0110	0000	0000
25	1111	1111	0000	0101	0000	0011	0101	1000	0000
26	1111	1111	0001	0101	0100	0000	0010	0000	1001
27	1111	1111	0100	1111	0000	1101	1101	0000	0000
28	1111	1111	0000	0101	0000	0010	0111	0000	0000
29	1111	1111	0111	0101	0000	0000	0100	0000	0101
30	1111	1111	0000	0101	0000	0000	0000	1001	0000

J = Jarque Bera Test, L = Lilliefors Test, C =  $\chi^2$  Test, S = Shapiro-Wilk / Shapiro-Franca Test  
 0 = Test does not reject null hypothesis that the data is normal distributed  
 1 = Test rejects null hypothesis

Table 5.1: Normality tests (significance level 5%) of noise data based on the whole measurement in (a) and based on section of 100 samples in (b).

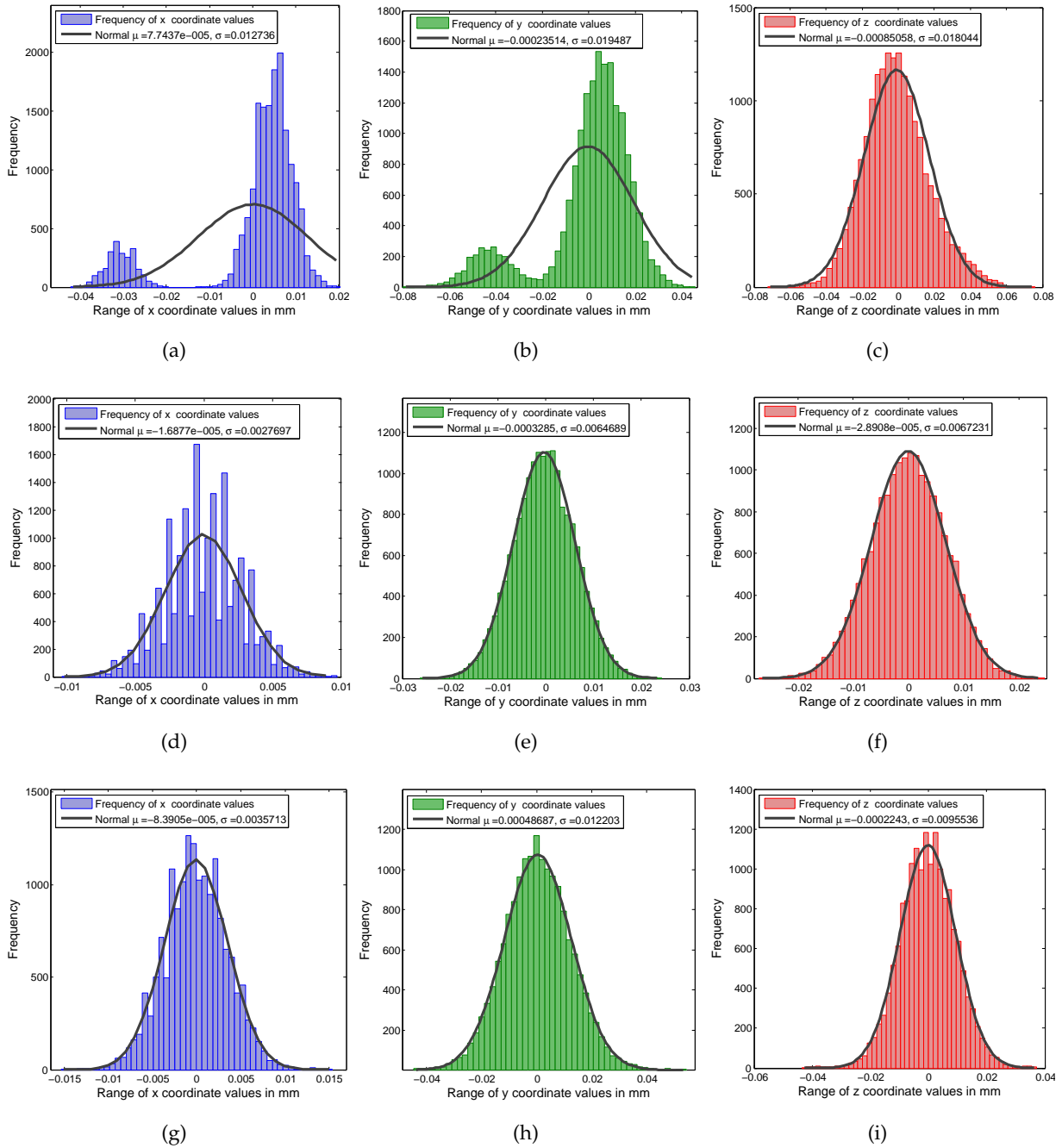


Figure 5.7: Exemplary histograms of floor marker coordinates for one measurement: (a)-(c) *Marker3*, (d)-(f) *Origin*, (g)-(i) *Trigger*.

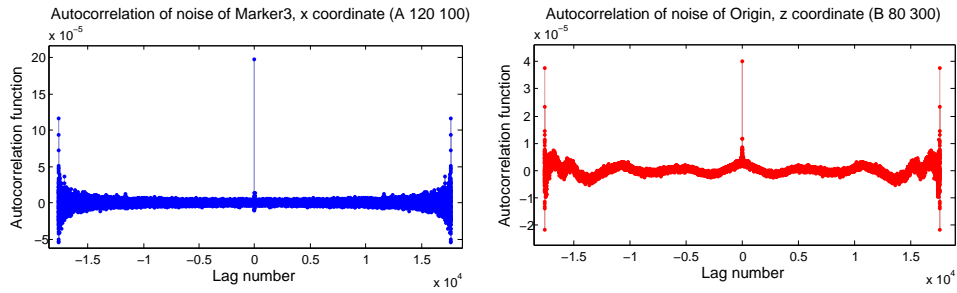


Figure 5.8: Exemplary autocorrelation functions of floor marker noise.

### 5.1.1.3 Whiteness

White noise is theoretically defined as a random signal which has a constant amplitude of its power spectral density for all frequencies. Hence, its total power is infinite. In practise, the bandwidth of a signal is finite and noise is considered as white if the power spectral density is flat within a fixed bandwidth. Processing of digital signals is covered in various introductory books, see for instance [Grü04].

The power spectral density function of a signal is the fourier transform of the autocorrelation function of that signal (Wiener-Khinchin theorem). The autocorrelation function of a signal  $x$  describes its correlation with itself at different points in time, defined as  $R_{xx}[n_1, n_2] = E\{x[n_1]x[n_2]\}$ . Therefore, the autocorrelation function of perfect white noise is a delta function at time shift zero with factor infinity. This means the noise at a certain point in time is totally independent of noise at other points in time. In reality the autocorrelation function of a signal considered as white has an finite impulse at time lag zero and is flat but not zero for the other time lags.

To check the floor marker noise for whiteness, the autocorrelation functions were examined.<sup>2</sup> All of them show an extensive impulse at lag zero and are relatively flat elsewhere, except at both ends. These higher values at the ends result from considering very short parts of the sequences.

Figure 5.8(a) exemplifies the autocorrelation function of a noise measurement well fulfilling the whiteness requirements. On the other hand, some autocorrelation functions reveal periodicity, although they are relatively flat (see Figure 5.8(b)). These autocorrelations indicate less perfect white noise. To what extent the autocorrelations resembled that of perfect white noise varies

<sup>2</sup>The corresponding MATLAB function (*xcorr* with option *unbiased*) estimates the autocorrelation function by the sequence

$$R_{xx}(m) = \begin{cases} \frac{1}{N - |m|} \sum_{n=0}^{N-m-1} x_{n+m}x_n & m \geq 0 \\ R_{xx}(-m) & m < 0 \end{cases}$$

of length  $2 \cdot N - 1$ , where  $N$  is the length of  $x$ .

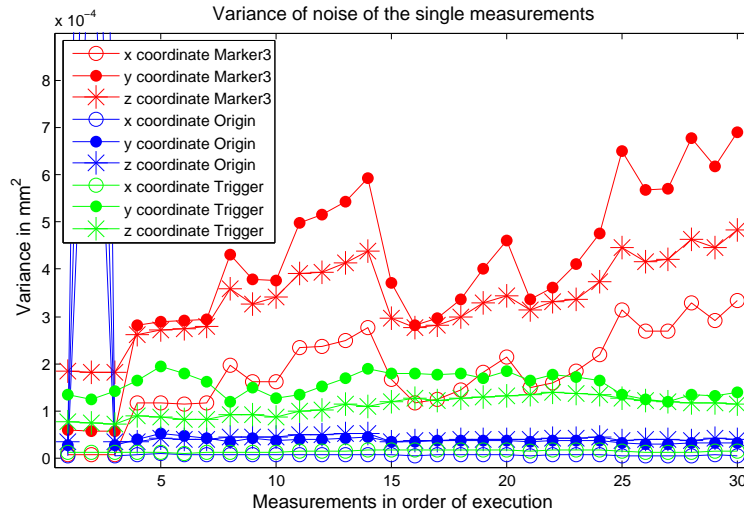


Figure 5.9: Variance per measurement determined for different markers and coordinates. (The variance of marker *Origin*'s noise of measurement 2 is  $1.2 \cdot 10^{-3} \text{ mm}^2$  for the *x*-coordinate,  $4.2 \cdot 10^{-3} \text{ mm}^2$  for the *y*-coordinate, and  $1.8 \cdot 10^{-3} \text{ mm}^2$  for the *z*-coordinate, .)

throughout the measurements. A dependence on the different coordinates and/or markers could not be revealed. Overall, it seems reasonable to assume that the noise is white.

#### 5.1.1.4 Variance

For filtering techniques like Kalman Smoothers, the variance of the noise is needed as an input parameter. Henceforth, the variance of the noise measurements are determined and visualised in Figure 5.9.

The outstanding large variance of marker *Origin* during measurement 2 is reasonable when considering the underlying extremely noisy measurement, which was shown in Figure 5.3. The variance values concerning the other measurements of marker *Origin* are fairly constant, as should be expected.

The determination of marker *Trigger*'s noise involved the removal of a large number of outliers. Since the cut between its noise and the outliers is not absolutely clear, the identified variance for *Trigger* should be treated with caution.

The variance of *Marker3* is barely changing during the first three measurements. Beginning from the fourth measurement the variance takes much larger values which differ a lot in the course of the measurements. This is in conformity to the position data of *Marker3* as described in Section 5.1.1.1.

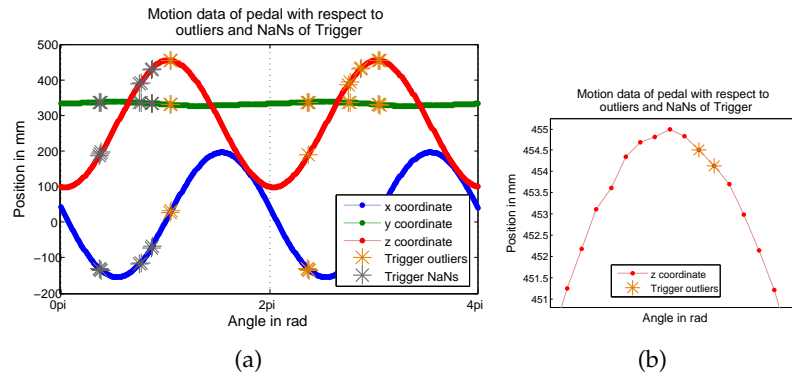


Figure 5.10: The motion of the pedal marker is observed with regards to outliers and NaNs of the respective *Trigger* data. (a) shows the behaviour for several crank revolutions, whereas (b) zooms in on a small section of it.

### 5.1.1.5 Applying Noise Characteristics to Pedal Motion

So far we focussed on the floor marker noise with regards to zero mean Gaussian distribution, whiteness and variance. The main inconsistencies are the type of noise affecting the  $x$ - and  $y$ -coordinates of *Marker3*, as well as the outliers concerning *Trigger*, but which are presumed to be caused by a motion.

Formal normality tests rejected a normal distribution for the  $x$ - and  $y$ -coordinates of *Marker3* and the histograms showed rather two Gaussian curves instead of one. For the other cases, a relatively Gaussian distribution might be assumed.

The noise data was separated from the measurements by subtracting the moving average. Clearly, this data determined as noise has about zero mean.

True white noise only exists theoretically. However, the autocorrelation functions of the floor marker noise show a clear impulse at zero lag and besides are relatively flat. This allows the assumption that this noise is fairly white.

It is intended to transfer characteristics of the noise affecting the floor marker onto the pedal motion data. But the noise of the pedal marker might exhibit anomalies as discovered for *Marker3* ( $x$ - and  $y$ -coordinate) as well, or it might be influenced by the same source producing the outliers of *Trigger*.

The author does not see a possibility to examine such types of noise and their characteristics for the pedal marker motion data. Henceforth, zero mean white Gaussian noise as revealed for most of the other floor marker measurements is assumed to be applicable for the pedal marker, too.

The variance of the noise differs between the measurements. Excluding the extreme values computed for the second measurement for marker *Origin*, the minimum variance value is  $4.97 \cdot 10^{-6} \text{ mm}^2$  and the maximum value is  $6.90 \cdot 10^{-4} \text{ mm}^2$ . The mean variance per coordinate over all measurements are  $8.16 \cdot 10^{-5} \text{ mm}^2$  for the  $x$ -coordinate,  $2.46 \cdot 10^{-4} \text{ mm}^2$  for the  $y$ -coordinate and

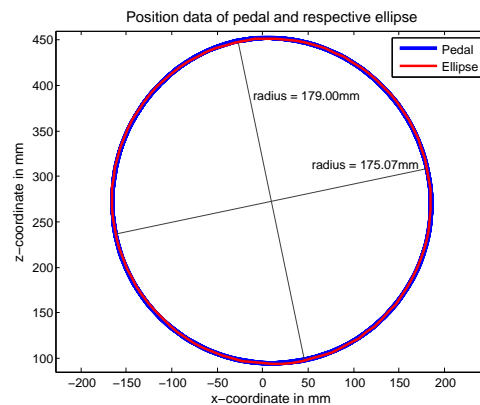


Figure 5.11: Motion of pedal marker and respective least squares ellipse.

$1.83 \cdot 10^{-4} \text{ mm}^2$  for the  $z$ -coordinate. Their average value over all coordinates is  $2.76 \cdot 10^{-5} \text{ mm}^2$ .

At last a look is taken at the motion data of the pedal itself. Figure 5.10(a) shows the pedal data which does not reveal noise at first glance. With a more precise look Figure 5.10(b) shows that the motion might not be as smooth as to expect. In both figures, outlier or NaN positions of marker *Trigger* are pointed out. They do not show a visually perceivable influence on the pedal motion, but this does not mean that no influence exists.

### 5.1.2 Instrumental Error

In reality the angular motion (velocity, acceleration) of the crank has to be regarded with respect to the bottom bracket position. Because of the structural conditions of the ergometer, it was refrained from placing a marker onto the bottom bracket and consequently its motion was not tracked.

As the ergometer setup was quite solid, it was expected that the bottom bracket would rarely change its central position while pedalling. Further, the material was assumed to be stiff such as deflection/torsion would not occur to a perceptible amount. Hence, the angular crank motion was computed with respect to the centre of the rotational movement of the pedal marker.

When analysing the trajectory of the pedal marker, it turned out that it did not follow a perfect circle, but was slightly ellipsoidal. Fitting the pedal data to the least squares ellipse<sup>3</sup> (after transforming the three-dimensional into two-dimensional data, as described in Section 5.2) is shown in Figure 5.11. The average radius of the shorter and the longer axis of the fitted ellipse are 17.50 cm and 17.88 cm, with a variance of  $0.0004 \text{ cm}^2$  and  $0.0012 \text{ cm}^2$  respectively. In contrast, the crank length was 17.50 cm.

<sup>3</sup>The fitting of the data to an ellipse was done using the MATLAB file `fit_ellipse.m` by Ohad Gal. Online: <http://www.mathworks.com/matlabcentral/fileexchange/3215> [Accessed 23. March 2009].

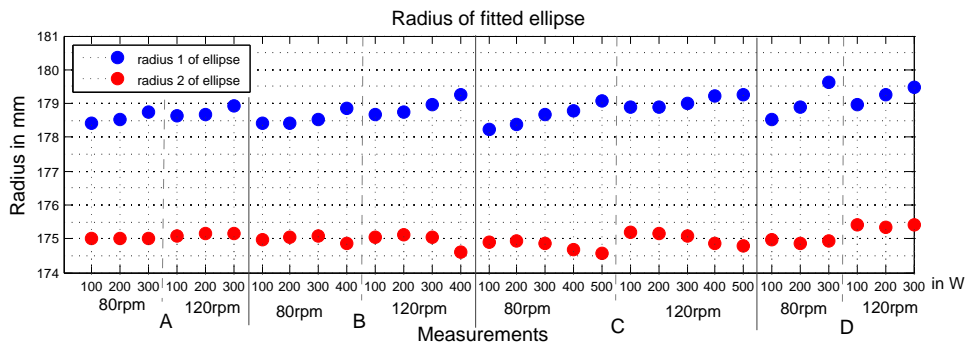


Figure 5.12: The smaller and larger radius of the fitted ellipses of the single measurements are plotted.

The radius of the fitted ellipse differs depending on cadence and power. A higher power level and likewise a higher cadence result in larger deviations from a perfect circle (see Figure 5.12).

The deviation from the expected circular motion occurs systematically at the same crank angles for all measurements, with its peaks at about the top and bottom death centre. As the deviation is systematic and since its magnitude is significant, it should not be due to measurement noise.

The ellipsoidal motion can have several possible reasons. There might have been some tolerance at the bottom bracket, allowing it to move slightly. Moreover, the ergometer might have moved as a whole. These two explanations imply a translational movement of the crank (and the bottom bracket), additional to its rotational motion. Then, the rotational motion about the centre of the circle/ellipse is not the same as the rotation about the slightly moving bottom bracket.

On the other hand, the marker might have been placed not perfectly on the pedal axis, with an inaccuracy not visible for the human eye. This would result in a slightly different angle for the marker with respect to that of the actual crank position.

The angle between pedal and crank is varying within the pedal cycle (see Figure 2.2). Thus, the trajectory of a marker not placed precisely on the pedal axis does not have to specify a perfect circle. Since the angle between pedal and crank was not measured, it could not be verified if the marker placement was a reason for the ellipsoidal movement.

The same problem can arise from deflection/torsion of the pedal.

When considering the motion of the pedal marker in three dimensions (see Figure 5.14), a slight motion within the  $y$ -dimension is detected. This is mainly due to the definition of the camera coordinate system, which is slightly askew to the sagittal plane of the pedal motion and which is removed by the transformations in Section 5.2.

A slight lateral motion of the pedal marker remains after the transformations, which means it must have been present in reality. Hence, this lateral motion might also be one cause of the ellipsoidal trajectory. It cannot be determined if only the pedal minimally moved sideways or if the crank moved as well.

Based on the information available it is not possible to identify the reason of the ellipsoidal motion of the pedal marker. It might originate from one of the possible explanations mentioned above, a combination thereof, or something else.

Since it might stem from a multitude of causes, no way was found to remedy this problem.

## 5.2 Preprocessing of Motion Data

The captured motion of the pedal marker is three-dimensional, but the actual movement of the crank nearly takes place only in two dimensions. For the computation of the tangential pedal force, the angular acceleration about the crank axis has to be determined. The slight lateral motion of the crank does not cause a torque and is hence discarded when transforming the three-dimensional pedal data into two-dimensional data.

The  $x$ - $z$ -plane of the camera coordinate system is not as parallel as possible to the sagittal plane of the main motion of the pedal marker. Therefore, first the plane is determined, which has a least squared distance to the pedal points (Section 5.2.1). This reduces the variations of the  $y$ -coordinate. Then the pedal points are projected onto this plane, and transformed into a respective two-dimensional coordinate system (Section 5.2.2).

At last, the centre of the rotational motion is translated into the origin of the coordinate system. The same operations have to be applied to marker *Trigger*, which is used to define the start of each crank revolution. The other two markers on the floor were only needed for the definition of the LUKOtronic coordinate system and are not used for the further computations.

A three-dimensional view of the original displacement data is shown in Figure 5.13 and a one-dimensional view before and after the transformations in Figure 5.14.

### 5.2.1 Determination of Least Squares Plane

The optimal least squares plane  $E$  minimising the average squared distance to the pedal points is computed using the MATLAB file *lsqPlane.m*<sup>4</sup> of Ofek Shilon. Subsequently, the working of this file will be depicted. A description of the underlying method can inter alia be found in [Nie94].

---

<sup>4</sup>The MATLAB files *lsqPlane.m* and *lsqAffineSpace.m* are available at: <http://www.mathworks.com/matlabcentral/fileexchange/loadFile.do?objectId=11920&objectType=File> [Accessed 01. April 09].

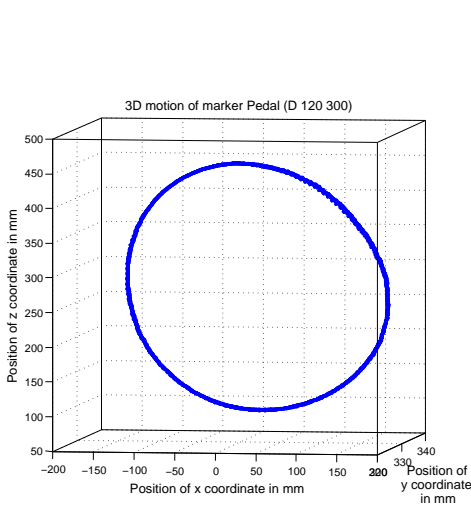


Figure 5.13: Three-dimensional motion of the pedal (pedal3D).

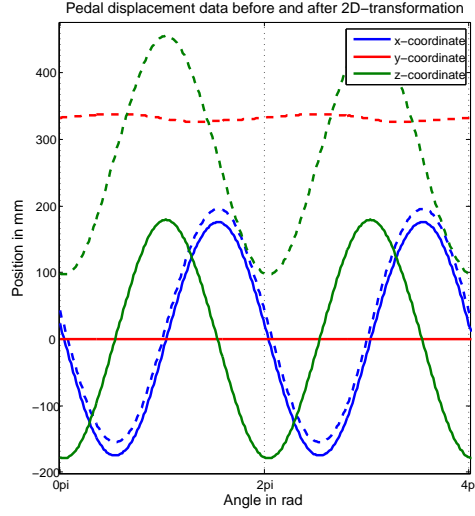


Figure 5.14: The dashed lines are the measured displacement data, whereas the continuous lines show the data after 2D transformation.

Plane  $E$  is defined by a point  $e$  in the plane and a normal vector  $v$ . An optimal subspace has to contain the centre of mass [You37]. Thus, the centre of mass (which is the mean of all  $n$  pedal points) can be used as point  $e$  of the optimal plane:

$$\mathbf{e} = \frac{1}{n} \sum_{i=1}^n \text{pedal3D}_i, \quad (5.1)$$

where  $\text{pedal3D}$  denotes the  $3 \times n$ -matrix of the three-dimensional pedal data. The normal vector  $v$  has to be chosen in such a way as to minimise the sum  $D$  of squared distances between the pedal points and plane  $E$ :

$$D(\mathbf{v}, \mathbf{e}; \text{pedal3D}_1, \dots, \text{pedal3D}_n) = \sum_{i=1}^n \frac{\langle \text{pedal3D}_i - \mathbf{e}, \mathbf{v} \rangle^2}{\|\mathbf{v}\|^2}, \quad (5.2)$$

whereas  $\langle \cdot, \cdot \rangle$  stands for the scalar product and the vector norm  $\|\cdot\|$  denotes the Euclidean norm  $\|\cdot\|_2$ .

A matrix  $\mathbf{Y}$  is defined as follows:

$$\mathbf{Y} = \begin{pmatrix} \text{pedal3D}_1 - \mathbf{e} \\ \vdots \\ \text{pedal3D}_n - \mathbf{e} \end{pmatrix}. \quad (5.3)$$

The sum  $D$  is minimised by choosing the normal vector  $v$  which is the eigenvector of matrix  $\mathbf{Y}^T \mathbf{Y}$  corresponding to the smallest eigenvalue.

The normal vectors  $\mathbf{v}$  computed for the different measurements differ only very slightly in their absolute values. This is to be expected, as the position of the bicycle ergometer and the motion capture system have not been changed between the measurements.

### 5.2.2 Transformation into 2D Coordinate System

For the transformation into a two-dimensional coordinate system, first the pedal points `pedal3D` are projected parallel onto plane  $E$ , which was defined above. Then two orthogonal direction vectors in plane  $E$  are used to define the two-dimensional coordinate axes  $x$  and  $z$ .

Since plane  $E$  was slightly skew with respect to the  $x$ - $z$ -plane of the three-dimensional coordinate system, the  $x$  and  $z$  axes of the two- and the three-dimensional coordinate system are similar but not equal.

For a more useful representation of the rotational motion and the ease of the crank angle computation, the centre of the motion is moved to the origin of the coordinate system.

Marker *Trigger* was fixed on the floor underneath the bottom bracket for the identification of the beginning of the pedal cycle. For the respective computations the mean value of this marker is used.

Before determining the mean, outliers are removed (see Section 5.1.1.1). Then this mean is transformed into the two-dimensional coordinate system.

## 5.3 Smoothing

The importance of smoothing noisy measurement data is demonstrated in Figure 5.15. The angular velocity (Figure 5.15(a)) obtained without smoothing is quite noisy, but the angular acceleration (Figure 5.15(c)) is so noisy that no meaningful information is detectable.

The translational velocity (Figure 5.15(b)) and acceleration (Figure 5.15(d)) are far less noisy than the angular ones. Higher noise in the angular data results from the angle determination based on the position data. By the combination of the  $x$ - and  $z$ -coordinate (i.e., the computation of the angles) the noise of both coordinates is not simply added but more strongly increased [Cha08].

Smoothing techniques usually perform best if the measurement noise is zero mean, white, additive, and stationary. To some degree, nonlinear transformations destroy these properties [Wol95]. Therefore, the measurement data is first smoothed and the angles are calculated afterwards.

To determine the amount of smoothing necessary to yield proper derivatives, it is useful to examine the signal in the frequency domain. The amplitude spectrum of the pedal position data is considered in Section 5.3.1.

As mentioned in the introduction, filtering techniques differ in performance regarding different signals. Thus, smoothing was carried out by three tech-

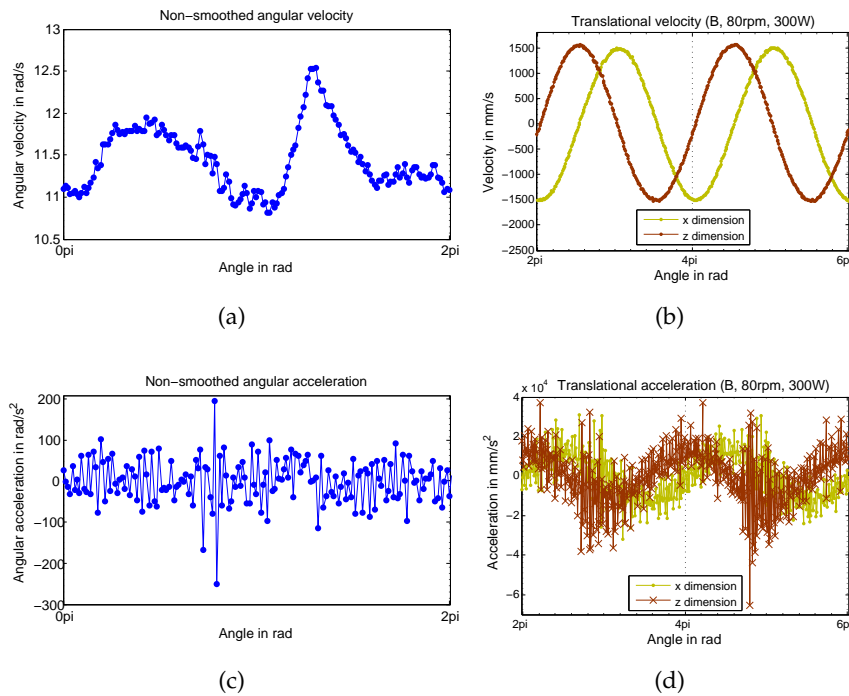


Figure 5.15: Angular velocity (a) and acceleration (c) and translational velocity (b) and acceleration (d) of crank for one pedal cycle without prior smoothing of the measurement data.

niques: a Butterworth filter (Section 5.3.2), a Kalman smoother (Section 5.3.3), and singular spectrum analysis (Section 5.3.4).

All techniques require the definition of certain parameters, as the cutoff frequency for the Butterworth filter, measurement and process noise covariance for the Kalman smoother, and the window size and the number of principal components used for reconstruction for singular spectrum analysis.

Methods for (semi-) automatically determining these parameters were used, but for the Butterworth filter, the respective results were bad. Hence, for the Butterworth filter the cutoff frequency was determined by hand to yield meaningful acceleration estimates.

As reported by Giakas and Baltzopoulos, the optimal cutoff frequency depends on the order of the derivative [GB97]. The higher the derivatives, the stronger is the noise amplification effect. A cutoff frequency that yields an optimal 0th derivative (i.e., the smoothed signal itself) is usually higher than the cutoff frequency for the first derivative, which in turn is higher than that for an optimal second derivative.

Often the optimal smoothing parameters are determined empirically by considering the true angular acceleration signal. This cannot be done here since the true acceleration is not available. Thus, three smoothing strategies were followed, providing a low, medium, or high level of smoothing.

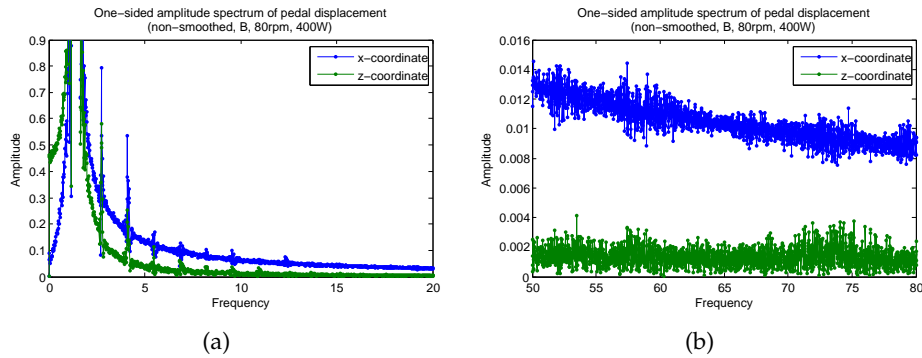


Figure 5.16: Amplitude spectrum of the pedal position data for measurements with cadence of 80 rpm and power 400 W. The amplitude of the fundamental frequency (not visible in the figure) is approximately 145.

The data was smoothed one-dimensional by treating  $x$ -coordinate and  $z$ -coordinate separately.

### 5.3.1 Amplitude Spectrum

In this section the amplitude spectrum of the pedal position data (after the transformations of Section 5.2) is examined. Exemplarily a spectrum of a measurement with a cadence of 80 rpm and power 400 W is shown in Figure 5.16.

The fundamental frequency is the average number of pedal revolutions per second. Its amplitude is considerably larger than all others. The second and third harmonic, although much smaller, are still clearly obvious. Further harmonics are detectable, but those do not stand out from the noise that clearly. In general, all measurements show the main characteristics of the examples in Figure 5.16. Because of the difference in cadence, the same number of harmonics covers a larger frequency range for measurements with a higher cadence than for those with a lower cadence.

The noise inherent in the pedal spectrum was assumed to be white and have very small amplitudes. This noise is not known directly but assumed to be similar to the noise affecting the markers on the floor (see also Section 5.1.1). An exemplary amplitude spectrum of a floor marker is considered in Figure 5.17. The amplitudes for the whole frequency range are very small and rather flat.

Nonetheless, regarding the amplitude spectrum of the pedal position data, even very high frequencies show detectable variations of their amplitudes (see Figure 5.16(b)). It cannot be resolved clearly whether these frequencies contribute to the true signal or whether they are part of the noise.

The higher the frequency the more likely the smoothing procedures will remove them. In case those amplitudes belong to the true signal, their contribution will decrease with their amplitude (which in turn decreases with the

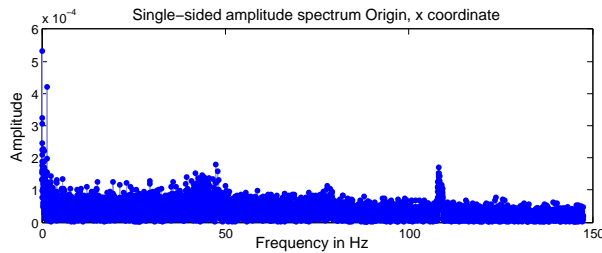


Figure 5.17: Amplitude spectrum of floor marker Origin (after its mean had been removed). Please consider the different scaling of the ordinate with respect to Figure 5.16.

frequency for our measurements). On the other hand, if these frequency variations (Figure 5.16(b)) are part of the noise, then, in contrast to the above assumptions, this noise is not white.

### 5.3.2 Butterworth Filter

A 2nd order low-pass Butterworth filter (BF) was used first in forward direction, then in reverse direction on the once-filtered data. This forward-backward filtering cancels out the phase lag introduced by the first filter operation and sharpens the cutoff to a 4th order filter.

The only parameter that has to be chosen besides the filter order is the cutoff frequency. It was attempted to determine the cutoff frequency using an automatic procedure proposed by Challis [Cha99], which is based on the autocorrelation of the residuals. For the pedal motion data the proposed cutoff frequency turned out to be much too high.

Due to the failure of the automatic procedure, the cutoff frequency was determined by trial and error, based on visual inspection of the amplitude spectrum and the smoothed and non-smoothed curves of the position data and the resulting angular velocity and acceleration.

Since the true angular acceleration is not known, it is not possible to determine which is the one best cutoff frequency. Thus, three cutoff frequencies were chosen, providing a rather low (cutoff frequency of 15 Hz), moderate (8 Hz), or high (4 Hz) amount of smoothing.

As a matter of completeness, the automatic procedure will be pointed out shortly, and the reason of its failure for the present motion data will be discussed.

#### Automatic Determination of Cutoff Frequency

Let  $f(t)$  be the original signal, which is composed of a true underlying signal and random noise. Further let  $f'(t)$  denote the filtered version of the original signal. The residual  $r(t)$  is the difference between the smoothed and the non-

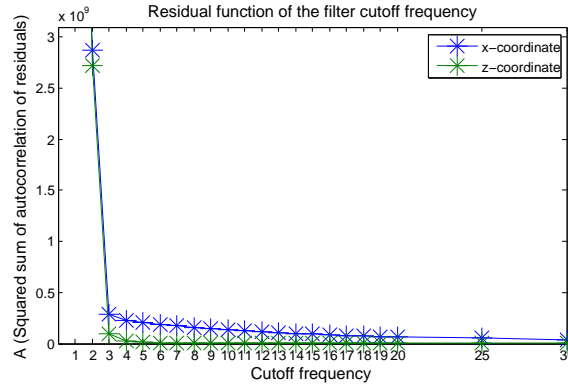


Figure 5.18: Function  $A$  for the automatic determination of the cutoff frequency. The first value (not shown) is  $7 \cdot 10^{11}$  and for increasing (not shown) cutoff frequencies, the value of function  $A$  further decreases.

smoothed signal:

$$r(t) = f'(t) - f(t). \quad (5.4)$$

If filtering produces a perfect separation of the true signal and the noise, than the noise is  $r(t)$ . As mentioned in Section 5.1.1.3, the autocorrelation function of perfect white noise is zero for all lag values not equal to zero.

Based on the assumption that the signal's noise is white, function  $A$  is defined as follows:

$$A = \sum_{l=1}^m R(l)^2, \quad (5.5)$$

where  $R(l)$  denotes the autocorrelation function of  $r(t)$  and  $l = 1, \dots, m$  the lag number. For a perfectly white signal  $A$  would be zero. Function  $A$  is computed iteratively on the residuals  $r(t)$  resulting from different cutoff frequencies. Assuming white noise, the optimal cutoff frequency is found as the one yielding the minimum value of  $A$ .

The values of function  $A$  for different cutoff frequencies are shown for one of our measurements in Figure 5.18. Low cutoff frequencies  $\leq 3$  Hz result in very high values for  $A$ . For our measurements, the higher the cutoff frequencies chosen, the smaller is the value of  $A$ .

The automatic procedure hence proposes a very high cutoff frequency. However, smoothing with a very high cutoff frequency (or even no smoothing at all) does not provide valuable angular acceleration estimates (see Figure 5.15(c)).

### Failure of Automatic Cutoff Determination

The procedure for automatically determination of the cutoff frequency is based on the autocorrelation of the residual function  $r(t)$  (5.4). Hence, its failure leads to the assumption that the residual function might not be white.

The visual inspection of the residuals confirms this assumption. Figure 5.19

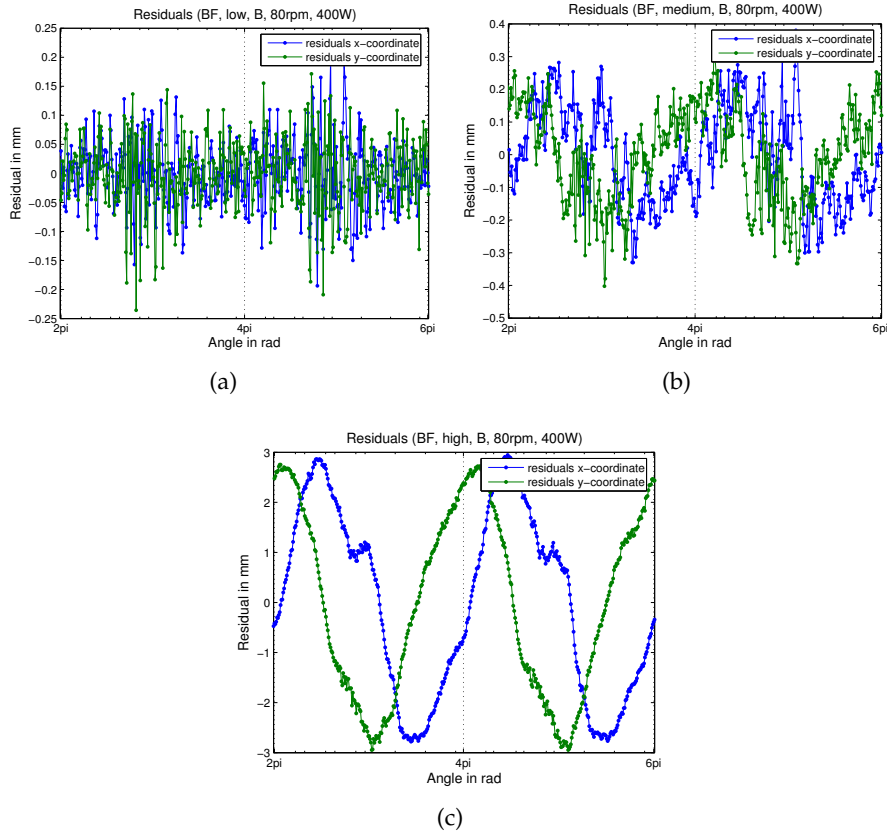


Figure 5.19: Residuals resulting from smoothing the pedal motion data using a Butterworth filter with a cutoff frequency of (a) 15 Hz, (b) 8 Hz, and (c) 4 Hz

shows the residuals corresponding to smoothing using a Butterworth filter with cutoff frequencies of (a) 15 Hz, (b) 8 Hz, and (c) 4 Hz. Periodicities are clearly observable and they are the more pronounced the lower the cutoff frequency.

In Figure 5.16(b) the amplitude spectrum of the corresponding measurement was shown. Since the amplitude spectrum is not that perfectly white even for very high frequencies, it becomes obvious that also the residual function  $r(t)$  is not white even for high cutoff frequencies.

### 5.3.3 Kalman Smoother

The Kalman filter (KF) is used for estimating the state of a dynamic system from noisy measurements. Basically, it filters the signal by recursively predicting the state ahead, followed by updating this state based on the respective noisy measurement. The Kalman filter is the optimal estimator for certain types of problems and a useful estimator for many further types [May79, Gel74].

A Kalman smoother (KS) estimates the states based on all measurements (i.e., not only the preceding ones). We use a fixed-interval Kalman smoother, which means a Kalman filter is applied once forward over the whole signal, and afterwards it is run backwards over the filtered signal. This makes use of all information possible and cancels out the phase lag introduced by the Kalman filter.

Our method basically follows the approach of Fioretti and Jetto [FJ89, FJ94], who proposed a Kalman smoother that obtains smoothed estimates of a signal and its derivatives simultaneously.

In the following, process model and Kalman filter will be adapted for a system of order  $m = 3$  (i.e., for determining smoothed position data, velocity and acceleration) and a one-dimensional signal. For the actual implementation, we chose  $m = 4$  since the higher the order, the smaller is the model error for the derivatives of lower order. A higher value could not be chosen, as this resulted in problems regarding computational accuracy (matrices became close to singular or badly scaled).

The method for the general case ( $m \geq 3$ ) can be found in [FJ89, FJ94]. For a thorough introduction to Kalman filtering see [GA08], for example.

### Process Model

In Kalman filtering the estimation of a state  $\mathbf{X}$  is based on the linear stochastic difference equation of the process:

$$\mathbf{X}(kT + T) = \mathbf{A}\mathbf{X}(kT) + w(kT), \quad (5.6)$$

and the measurement

$$y(kT) = \mathbf{C}\mathbf{X}(kT) + v(kT). \quad (5.7)$$

The  $m \times m$  matrix  $\mathbf{A}$  relates the previous state to the current state, and  $w$  is a scalar white noise process termed process noise. Matrix  $\mathbf{C}$  couples the state  $\mathbf{X}(kT)$  to the measurement  $y(kT)$ , and the white noise sequence  $v \sim \mathcal{N}(0, \sigma_v^2)$  denotes the measurement noise.

Our Kalman smoother shall estimate the position  $p$ , velocity  $s$ , and acceleration  $a$  of the crank. Hence, the resulting state vector is

$$\mathbf{X}(kT) = \begin{bmatrix} p(kT) \\ s(kT) \\ a(kT) \end{bmatrix}, \quad (5.8)$$

and the state transition matrix is

$$A = \begin{bmatrix} 1 & T & \frac{T^2}{2} \\ 0 & 1 & T \\ 0 & 0 & 1 \end{bmatrix}, \quad (5.9)$$

where  $T$  denotes the time interval between two measurements. Since the only measured data is the position, the input coupling matrix is  $\mathbf{C} = \begin{bmatrix} 1 & 0 & 0 \end{bmatrix}$ .

Thus, the resulting model is:

$$\begin{bmatrix} p(kT + T) \\ s(kT + T) \\ a(kT + T) \end{bmatrix} = \begin{bmatrix} 1 & T & \frac{T^2}{2} \\ 0 & 1 & T \\ 0 & 0 & 1 \end{bmatrix} \cdot \begin{bmatrix} p(kT) \\ s(kT) \\ a(kT) \end{bmatrix} + w(kT), \quad (5.10)$$

$$y(kT) = \begin{bmatrix} 1 & 0 & 0 \end{bmatrix} \cdot \begin{bmatrix} p(kT) \\ s(kT) \\ a(kT) \end{bmatrix} + v(kT). \quad (5.11)$$

Fioretti and Jetto [FJ89] showed that the process noise  $w(kT)$  can be modelled as a white noise sequence  $\sim \mathcal{N}(0, Q)$ , with

$$Q = \sigma_w^2 \begin{bmatrix} \frac{1}{20}T^5 & \frac{1}{8}T^4 & \frac{1}{6}T^3 \\ \frac{1}{8}T^4 & \frac{1}{3}T^3 & \frac{1}{2}T^2 \\ \frac{1}{6}T^3 & \frac{1}{2}T^2 & T \end{bmatrix} \quad (5.12)$$

(with respect to our model of order  $m = 3$ ).

### Operation of the Kalman Smoother

The Kalman filter operates in two steps, which are predicting a state and then correcting it. This is based on the *a priori* and *a posteriori* estimate error covariance. The former denotes the covariance of the error between the predicted and the true state, whereas the latter corresponds to the error between the corrected and the true state. The Kalman gain is a factor which is chosen to minimise the *a posteriori* error covariance.

Generally the error covariance and the Kalman gain are updated within each iteration of the Kalman filter. We chose a steady-state Kalman filter, since the Kalman gain remained constant after some time. The steady-state Kalman gain  $K$  and the *a posteriori* error covariance were determined beforehand by resolving corresponding discrete algebraic riccati equations, based on process and measurement noise covariances.

The Kalman smoother is based on a Rauch-Tung-Striebel two-pass smoother (see, for example [GA08]), but as a steady-state version. The first pass uses a Kalman filter, whereas the second pass determines the smoothed state estimates from intermediate results of the forward pass. For the respective algorithm see [FJ89, FJ94].

### Determination of Measurement and Process Noise Covariance

An attempt was made to estimate measurement and process noise covariance using a method proposed by Fioretti and Jetto [FJ94].

Their method is based on variance matching between the theoretical and the observed autocorrelation function of the innovation process. The innovation process denotes the residual sequence of the noisy measurements and their optimal estimates produced by a Kalman Filter.

This approach failed for our measurements, due to the same reasons discussed above for the automatic cutoff frequency determination for the Butterworth filter. Hence, this approach had to be discarded as well.

Since the automatic method failed, measurement and process noise covariance had to be determined elsewhere. The measurement noise variance cannot be determined based on the noisy pedal motion data. It was assumed that the measurement noise variance was similar to the variance of the markers on the floor.

Hence, the mean variance per coordinate over all measurements of the floor markers are chosen as the measurement noise variance (see Section 5.1.1.4 and 5.1.1.5), which is  $8.16 \cdot 10^{-5} \text{ mm}^2$  for the  $x$ -coordinate and  $1.83 \cdot 10^{-4} \text{ mm}^2$  for the  $z$ -coordinate.

The process noise covariance had already been defined above, except the multiplicative skalar  $\sigma_w^2$ . Fioretti and Jetto [FJ89] proposed a method for estimating an upper bound based on the signal spectrum and the assumption that the signal is band-limited. They state that signals are not band-limited in reality, but that practically in most cases the signal spectrum above a band-limit can be neglected.

The formula for the estimation of  $\sigma_w^2$  requires the signal spectrum and the definition of the band-limit. However, for the pedal motion data a clear band-limit could not be defined. Different band-limits were tried, defined as multiples of the fundamental frequency  $ff$ . This results in different cutoff frequencies for different measurements, depending on their fundamental frequency. Approximately the same amount of smoothing resulted for the different measurement with respect to a chosen multiple. For the further analysis three multiple were determined, resulting in a low ( $15 \cdot ff$  Hz), medium ( $10 \cdot ff$  Hz) and high low ( $5 \cdot ff$  Hz) degree of smoothing.

### Remarks Regarding the Determination of Angular Velocity and Acceleration

Smoothing both one-dimensional signals ( $x$ - and  $z$ -coordinate) using the Kalman smoother yields a smoothed version of the original position data and smooth translational velocities and accelerations for the  $x$ - and  $z$ -coordinate separately.

There are two obvious possibilities for computing the angular velocity and acceleration of the crank. One is to calculate the derivatives of the crank angles, which in turn are determined based on the smoothed position data, as described in Section 5.4.

Another approach is to obtain the angular velocity and acceleration directly from the translational velocities. Transforming the translational velocities  $\mathbf{v}_x(t)$  and  $\mathbf{v}_y(t)$  into polar coordinates results in a conjoint representation by angle  $\varphi_v(t)$  and radius  $r_v(t)$ .

Since the velocity is rectangular to the position data,  $r_v(t)$  gives the tangential velocity  $v_t(t)$  of the rotational motion. The angular velocity  $\omega(t)$  is determined as  $\omega(t) = \frac{v_t(t)}{r_p(t)}$ , where  $r_p(t)$  denotes radius of rotational motion at time  $t$  (i.e.,  $r_p(t)$  is the radius at time  $t$  of the position data when transformed into polar coordinates).

Then the angular acceleration was obtained as the first derivative of the angular velocity. This approach produced the same results as the one based on the position data only (see Section 5.4). Therefore, it was discarded.

### 5.3.4 Singular Spectrum Analysis

Singular spectrum analysis (SSA) is a rather novel technique of time series analysis, which can be used for trend extraction, smoothing, extraction of oscillatory components, and to obtain the structure of a series.

It is a model-free technique that is aimed at decomposing a time series into several additive components like a slowly varying trend, oscillatory components, and noise components.

When applying SSA for smoothing, the original signal is interpreted as being composed of two components: the true signal and the noise.

SSA consists of two complementary stages: *decomposition* and *reconstruction*. Each stage is further comprised of two steps, which are 1) *embedding*, 2) *singular value decomposition*, 3) *reconstruction*, and 4) *diagonal averaging*.

In the following the basic algorithm and subsequently the automatic filtering procedure used within this thesis are described. A thorough description of the theoretical foundations of singular spectrum analysis as well as practical examples can be found in the book of Golyandina et al. [GNZ01].

#### Basic SSA

##### Stage 1: Decomposition

###### Step 1: Embedding

The embedding step maps the one-dimensional original signal  $F = (f_0, \dots, f_{N-1})$  of length  $N$ ,  $N > 2$ , to a trajectory matrix  $\mathbf{X} = [X_1 : \dots : X_K]$  of lagged vectors  $\mathbf{X}_i$ .

A window of length  $L$  (*window length*),  $1 < L < N$  is slid over the signal  $F$ , forming  $K = N - L + 1$   $L$ -dimensional lagged vectors

$$\mathbf{X}_i = (f_{i-1}, \dots, f_{i+L-2})^T, \quad 1 \leq i \leq K.$$

Each lagged vector forms a column of the trajectory matrix:

$$\mathbf{X} = \begin{pmatrix} f_0 & f_1 & f_2 & \cdots & f_{K-1} \\ f_1 & f_2 & f_3 & \cdots & f_K \\ f_2 & f_3 & f_4 & \cdots & f_{K+1} \\ \vdots & \vdots & \vdots & \ddots & \vdots \\ f_{L-1} & f_L & f_{L+1} & \cdots & f_{N-1} \end{pmatrix}. \quad (5.13)$$

Thus, trajectory matrix  $\mathbf{X}$  is a Hankel matrix (i.e., elements on the diagonals  $i + j = \text{constant}$  are equal).

### Step 2: Singular value decomposition

The second step is the singular value decomposition (SVD) of the trajectory matrix  $\mathbf{X}$ .

Let  $\mathbf{S} = \mathbf{X}\mathbf{X}^T$ . Further, the eigenvalues  $\lambda_i$  of  $\mathbf{S}$  are considered in decreasing order ( $\lambda_1 \geq \cdots \geq \lambda_L$ ), and  $\mathbf{U}_1, \dots, \mathbf{U}_L$  denote the corresponding eigenvectors. Defining

$$\mathbf{V}_i = \mathbf{X}^T \mathbf{U}_i / \sqrt{\lambda_i}, \quad i = 1, \dots, d, \text{ and } d = \max\{i, \text{ such that } \lambda_i > 0\} \quad (5.14)$$

the SVD of matrix  $\mathbf{X}$  can be expressed as the sum of elementary matrices  $\mathbf{X}_i = \sqrt{\lambda_i} \mathbf{U}_i \mathbf{V}_i^T$  as

$$\mathbf{X} = \mathbf{X}_1 + \cdots + \mathbf{X}_d. \quad (5.15)$$

In SVD terminology  $\sqrt{\lambda_i}$  are referred to as *singular values*,  $\mathbf{U}_i$  as the *left* and  $\mathbf{V}_i$  as the *right singular vectors*. Their combinations  $(\sqrt{\lambda_i}, \mathbf{U}_i, \mathbf{V}_i)$  are called *eigen-triples* of matrix  $\mathbf{X}$ .

### Stage 2: Reconstruction

#### Step 3: Grouping

The aim of the grouping step is to separate additive components of the original signal by defining which of the elementary matrices  $\mathbf{X}_i$  are used for reconstruction. This selection (*grouping strategy*) depends on the type of application the SSA is used for.

In case of smoothing the grouping strategy is based on the assumption that those elementary matrices which hardly contribute to the norm of the original matrix represent noise, whilst the others are regarded as components of the true signal.

Since the eigen-triples are ordered by decreasing singular values (i.e., by decreasing contribution to the original matrix), the approximation of matrix  $\mathbf{X}$  consists of the first  $r$  elementary matrices:

$$\mathbf{X} = \mathbf{X}_1 + \cdots + \mathbf{X}_r, \quad (5.16)$$

where  $r$  denotes the number of elementary matrices which are considered as being part of the true signal.

#### **Step 4: Diagonal Averaging**

Since in practise the approximated matrix  $\mathbf{X}$  is no longer a Hankel matrix, the smoothed signal cannot be recovered directly. By means of diagonal averaging each of the matrices used for reconstruction (i.e.,  $\mathbf{X}_1, \dots, \mathbf{X}_r$ ) is transferred into a new signal of length  $N$ .

Let  $\mathbf{Y}$  be a  $L \times K$  matrix with elements  $y_{ij}, 1 \leq i \leq L, 1 \leq j \leq K$ . Then the  $k$ -th element of the new signal is obtained by averaging  $y_{ij}$  over all  $i, j$  such that  $i + j = k + 2$ . This is referred to as *diagonal averaging*.

The matrix resulting from diagonal averaging is the closest (with respect to the matrix norm) to the approximated matrix  $\mathbf{X}$  among all Hankel matrices. Finally, the total smoothed signal is obtained by adding the signals that were recovered for the first  $r$  elementary matrices.

#### **Automatic Filtering Procedure**

The basic SSA algorithm requires two parameters: the window length  $L$  (embedding step), and the elementary matrices used for reconstruction. The selection of these parameters depends on the data itself and on the type of analysis performed (a detailed discussion regarding parameter selection can be found in [GNZ01]).

A large window length might result in mixing trend components and noise components in the reconstruction. On the other hand, a small window length might extract the trend but mix other components.

An automatic filtering method proposed by Alonso et al. [ADCP04] was chosen, which is based on recursively applying SSA to remove noise gradually. As already mentioned, when using SSA for smoothing the grouping strategy is to select the first  $r$  components for the reconstruction. The automatic algorithm chooses the number  $r$  which accounts for 99.999% of the sum of the eigenvalues.

Alonso et al. chose the window length  $L$  arbitrarily, pointing out that the results regarding their test data were not very sensitive to the chosen window length. However, our pedal motion data was sensitive to the window length. Three different window lengths  $L$  were chosen, providing a low ( $L = 15$ ), medium ( $L = 50$ ), and high ( $L = 200$ ) degree of smoothing. The resulting angular velocities and accelerations differ significantly, as will be seen Figure 6.2.

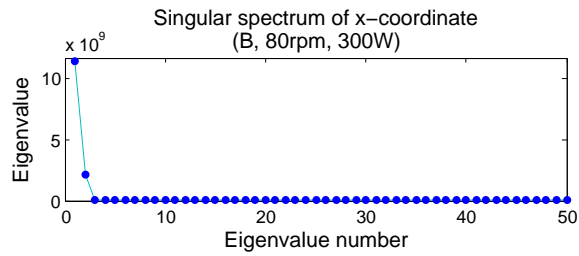


Figure 5.20: The first two eigenvalues of this singular spectrum have large values, whereas the others are much smaller. Window length  $L$  is 50 and the number  $r$  of components used for reconstruction is 2.

After choosing a window length  $L$ , the automatic method proceeds as follows for each iteration:

- apply SSA (reconstruction based on  $r$  which accounts for 99.999% of the sum of eigenvalues)
- calculate the acceleration signal
- stop if the difference between the root mean square values of the accelerations of two iterations is smaller than 1%, otherwise start new iteration based on the smoothed signal of the current iteration

When applying the automatic algorithm to our measurement data, about the first 2 to 4 components were used for reconstruction and about 1 to 4 iterations were carried out.

The exemplary singular spectrum shown in Figure 5.20 contains very high values for the first two eigenvalues and much lower values for all other eigenvalues. Since the first two eigenvalues account for 99.999% of the sum of the eigenvalues, only these two are chosen for reconstruction of the signal corresponding to Figure 5.20.

## 5.4 Derivative Estimation

After preprocessing (Section 5.2) and smoothing (Section 5.3) the crank angle is determined (Section 5.4.1). Then its first and second derivatives are numerically obtained by centred differences (Section 5.4.2).

### 5.4.1 Angular Position

The angular position of the crank is defined with respect to the centre of the angular motion of the pedal marker. As pointed out in Section 5.1.2, this inherent assumption of a fixed bottom bracket position might not be correct, but no better solution was found.

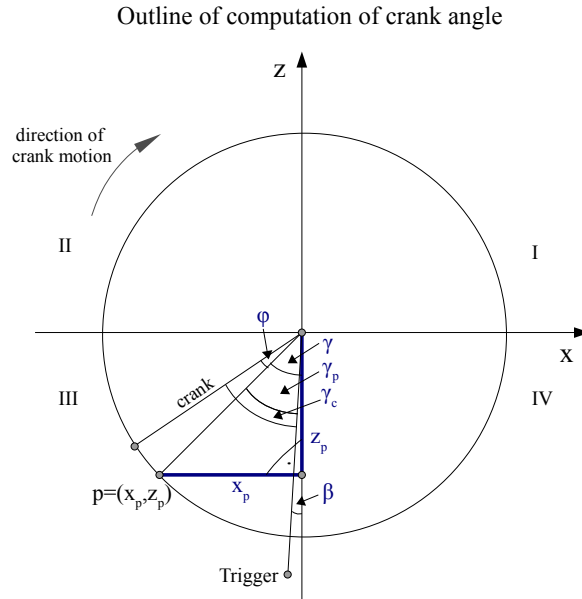


Figure 5.21: The crank angle is determined based on its offset  $\varphi$  to angle  $\gamma$  between the line from the origin to the pedal marker and the z-axis, and the offset  $\beta$  between the line from the origin to marker *Trigger* and the z-axis.

The angular position of the crank is obtained by first computing the angle  $\gamma$  between the line from the centre to the pedal marker position and the z-axis. This angle is corrected for the offset  $\beta$  between the marker *Trigger* and the z-axis and the offset  $\varphi$  between the pedal marker and the crank, see Figure 5.21.

The computation of angle  $\gamma$  between the pedal and the z-axis is based on:

$$\gamma = \arctan\left(\frac{x_p}{z_p}\right), \quad (5.17)$$

where  $x_p$  and  $z_p$  denote the  $x$  and  $z$  position of the pedal and the centre of the circular motion is the origin of the coordinate system. Dependent on the quadrant in which the pedal resides,  $\gamma$  follows from

$$\gamma = \begin{cases} \gamma + \pi & \text{if pedal in quadrant I or II,} \\ \gamma & \text{if pedal in quadrant III,} \\ \gamma + 2\pi & \text{if pedal in quadrant IV.} \end{cases} \quad (5.18)$$

The angle  $\beta$  between the line from the origin to marker *Trigger* and the z-axis is determined in the same way as  $\gamma$ . Marker *Trigger* was placed on the floor to indicate the bottom death centre of the pedal cycle, which is crank angle zero. If the coordinate system resulting after the preprocessing in Section 5.2 perfectly matches the world coordinate systems, angle  $\beta$  should be approximately zero. This is not the case, as the actual value of  $\beta$  is about  $4^\circ$ . Hence, to correct

this offset, angle  $\beta$  is subtracted from angle  $\gamma_p$ :

$$\gamma_p = (\gamma - \beta) \pmod{2\pi} . \quad (5.19)$$

The crank angle  $\gamma_c$  and the pedal marker angle  $\gamma_p$  are not the same due to a pedal rotation  $\varphi$  of  $11.7^\circ$ , as shown in Figure 3.4(b)<sup>5</sup>. Thus, to yield the crank angle  $\gamma_c$ , the offset  $\varphi$  has to be added to the angle  $\gamma_p$  of the pedal:

$$\gamma_c = (\gamma_p + \varphi) \pmod{2\pi} . \quad (5.20)$$

Finally, to obtain angles in increasing size, multiples of  $2\pi$  were added to angles  $\gamma_c$ , such that the values of the angles of the first revolution are between 0 and  $2\pi$ , that of the second between  $2\pi$  and  $4\pi$ , and so on.

#### 5.4.2 First and Second Derivatives

The angular velocity and acceleration are obtained by determining the first and second order centred difference of the angular position data. The angles are convolved with filter mask  $[0.5 \ 0 \ -0.5]$  for the first derivative and with  $[1 \ -2 \ 1]$  for the second derivative, followed by a division by the time difference and squared time difference respectively.

Longer filter masks, as described in [Jäh91], were tried as well, but they did not significantly improve the resulting derivatives.

---

<sup>5</sup>In Figure 3.4(b) the angle is  $12^\circ$ , since a different crank length was used.

## 6 Results and Discussion

This chapter first focusses on the obtained angular velocity and acceleration of the crank (Section 6.1), followed by the presentation and discussion of the resulting pedal force estimates (Section 6.2).

### 6.1 Angular Velocity and Acceleration

The main problem facing the evaluation of the acceleration estimates is that the true angular acceleration is not known. The non-smoothed angular acceleration (see Figure 5.15) is too noisy to consult. The non-smoothed angular velocity and the non-smoothed position data can be used to assess the degree of smoothing for the position data itself and the first derivative. However, the second derivative might need more smoothing than the first derivative, as mentioned in Section 5.3.

A quantitative analysis of the results is not possible since the true angular velocity and acceleration are not available. For our approach of pedal force computation only the angular acceleration but not the velocity is needed. Anyhow the angular velocity will be discussed since it will be used as an indicator of the quality of the derived angular acceleration and as it was used for the analysis in Section 2.2.3.

Angular velocity and acceleration estimates of all measurements show common characteristics depending on chosen cadence and power. A detailed examination of all 30 measurements would be too extensive. Hence, a short section of one measurement is exemplarily discussed, and thereby general observations are outlined.

It should be noticed that the smoothing parameters of the three techniques were determined semi-automatically and only yield approximately the same level of smoothing. Hence, differences in the resulting derivatives are not solely due to the smoothing techniques, but depend even stronger on the precise parameters chosen for a certain technique and measurement.

#### 6.1.1 Examination of Exemplary Measurement

A measurement with a cadence of 80 rpm and a power level of 200 W is exemplarily examined with respect to the three smoothing techniques and the three degrees of smoothing.

### Position Data

Deviations between smoothed and non-smoothed position data are rarely perceptible at other positions than the peak / low point. The smoothed and non-smoothed position data is shown in Figure 6.1 for a small sector of a peak. The lower the degree of smoothing, the more the smoothed data resembles the non-smoothed data.

For the highest level of smoothing chosen (Figure 6.1(c)), the smoothed data is clearly flattened, not reaching the peak values of the non-smoothed data. This is particularly pronounced in case of the Butterworth Filter.

### Crank Angular Velocity

The resulting crank angular velocity and acceleration profiles are shown in Figure 6.2. For a low degree of smoothing (Figure 6.2(a)), the smoothed angular velocity curves follow also minor changes in the non-smoothed velocity.

A medium level of smoothing (Figure 6.2(c)) still comprises the minor peak of the non-smoothed angular velocity curve at about an angle of  $4\pi$  rad (i.e., the respective crank position is the bottom dead centre). Smaller changes are not followed, and the two major peaks and low points are reached fairly well.

For a high degree of smoothing (Figure 6.2(e)) the smoothed angular velocity curve only follows the major curve of the non-smoothed velocity. Peaks and low points are flattened.

The non-smoothed angular velocity gives an idea about the true angular velocity, but it remains unsolved which of the minor deviations are due to fluctuations in the true velocity and which are due to noise.

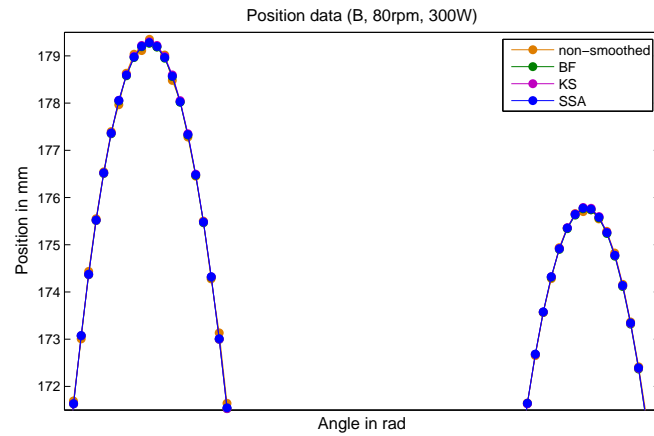
With respect to the non-smoothed angular velocity, a low and medium amount of smoothing seem to give a reasonable estimation of the true angular velocity, whereas the high degree of smoothing seems to cause oversmoothing.

### Crank Angular Acceleration

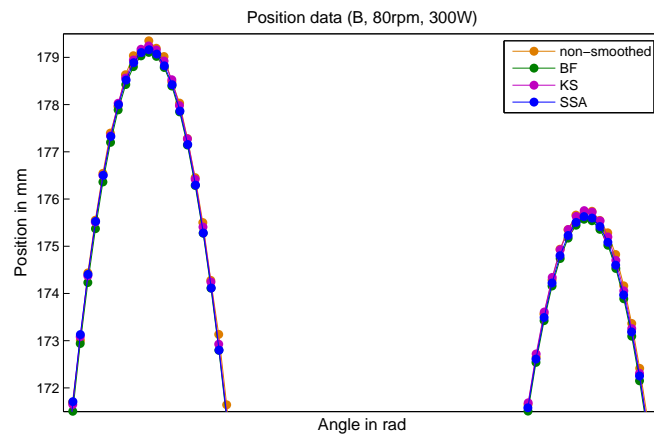
Differences between smoothing techniques and levels of smoothing are far more pronounced for angular acceleration than for angular velocity (see Figure 6.2). The lower the degree of smoothing, the stronger are the oscillations of the angular acceleration and the higher are its peaks.

For a medium level of smoothing (see Figure 6.2(d)) minor oscillations are removed, but the bending of the curve at about the bottom dead centre position of the crank (i.e., at  $4\pi$  rad in Figure 6.2(d)) persists. In the exemplary measurement this minor peak is only eliminated in the case of the highest smoothing tested, which was singular spectrum analysis (see Figure 6.2(f)). This involves strongly flattened peaks.

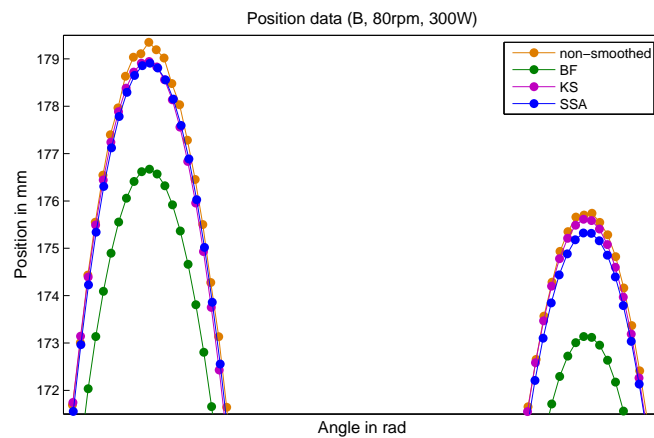
Theoretically, the angular acceleration curve of the crank is expected to be smooth and to show two peaks and low points per pedal cycle. The edge in the curve at the bottom dead centre (i.e., at a crank position of multiples of  $2\pi$  rad) is too obvious as to resulting from measurement noise.



(a)



(b)



(c)

Figure 6.1: Position data before and after smoothing with the three smoothing techniques. In (a) a low level of smoothing was chosen, in (b) a medium degree, and in (c) a high degree.

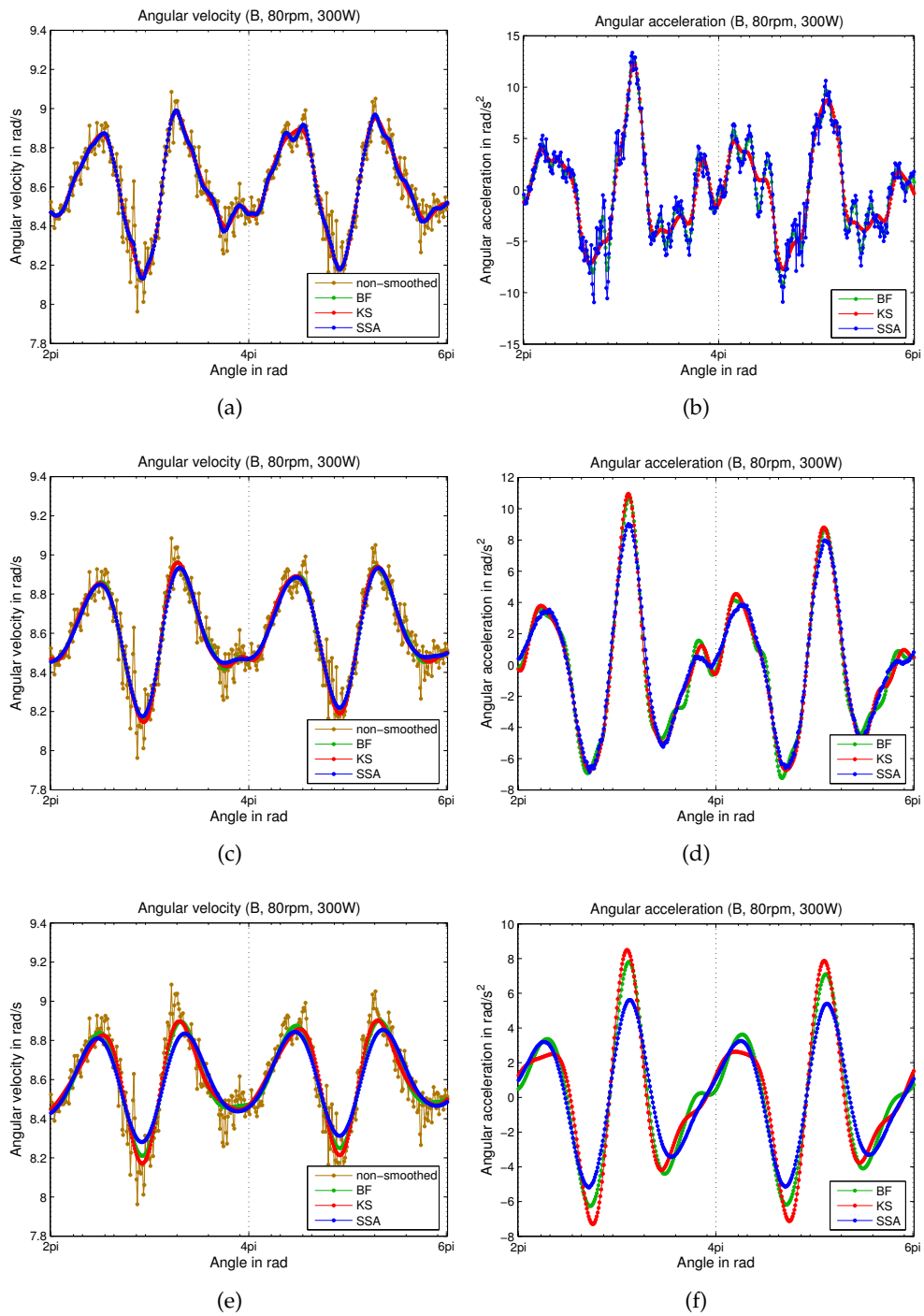


Figure 6.2: Crank angular velocity profiles are shown on the left and angular acceleration on the right. The degree of smoothing was low on the top ((a) and (b)), medium in the middle ((c) and (d)), and high on the bottom ((e) and (f)).

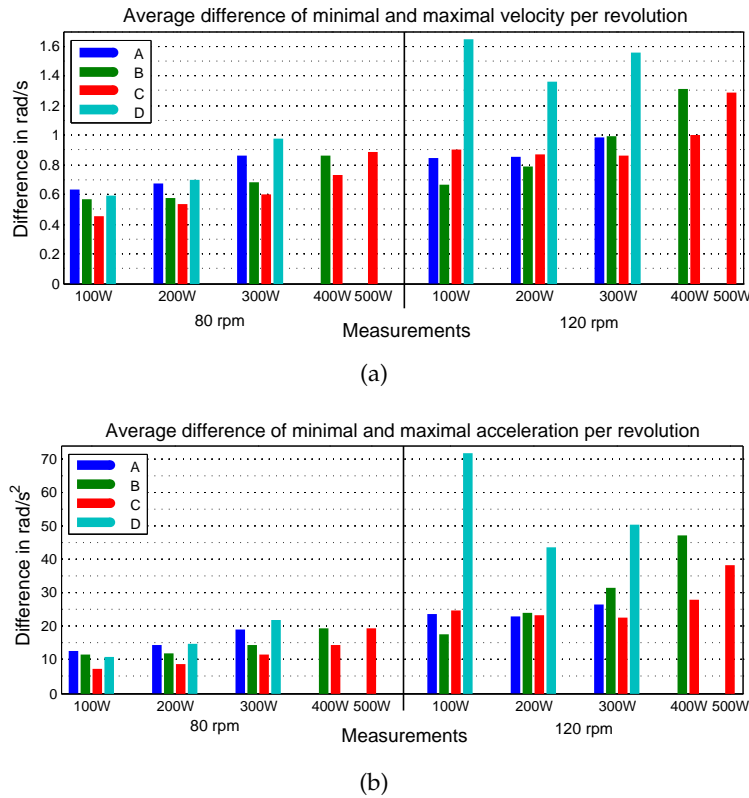


Figure 6.3: The average difference of minimal and maximal angular velocity (a) and acceleration (b) per revolution is shown for the 30 measurements. The underlying position data was smoothed using singular spectrum analysis and a medium degree of smoothing.

Since the true angular acceleration is not available it cannot be clarified whether the edge represents changing of the true angular acceleration, or if it results from something else, such as mechanical reasons. This matter will be discussed further in Section 6.2 with respect to the pedal force obtained from the Powertec System.

### 6.1.2 Dependency on Power and Cadence

Angular velocity and acceleration profiles of all measurements are generally similar regarding their shape. They differ in their amplitudes (i.e., the difference between the peak and the low point) with respect to the power levels and cadence.

As depicted in Figure 6.3, higher power tends to result in higher amplitudes, as does higher cadence. Regarding that figure it has to be kept in mind that, when conducting the experiments, claimed power levels and cadence were only met approximately. Hence, the measurements are only roughly comparable with respect to power and cadence.

## 6.2 Pedal Force Estimates

The pedal force obtained using motion capturing differs significantly from the pedal force measured by the Powertec System. Figure 6.4 shows the respective force profiles of the exemplary measurement discussed in the last section. Due to the wide discrepancy a quantitative analysis was omitted.

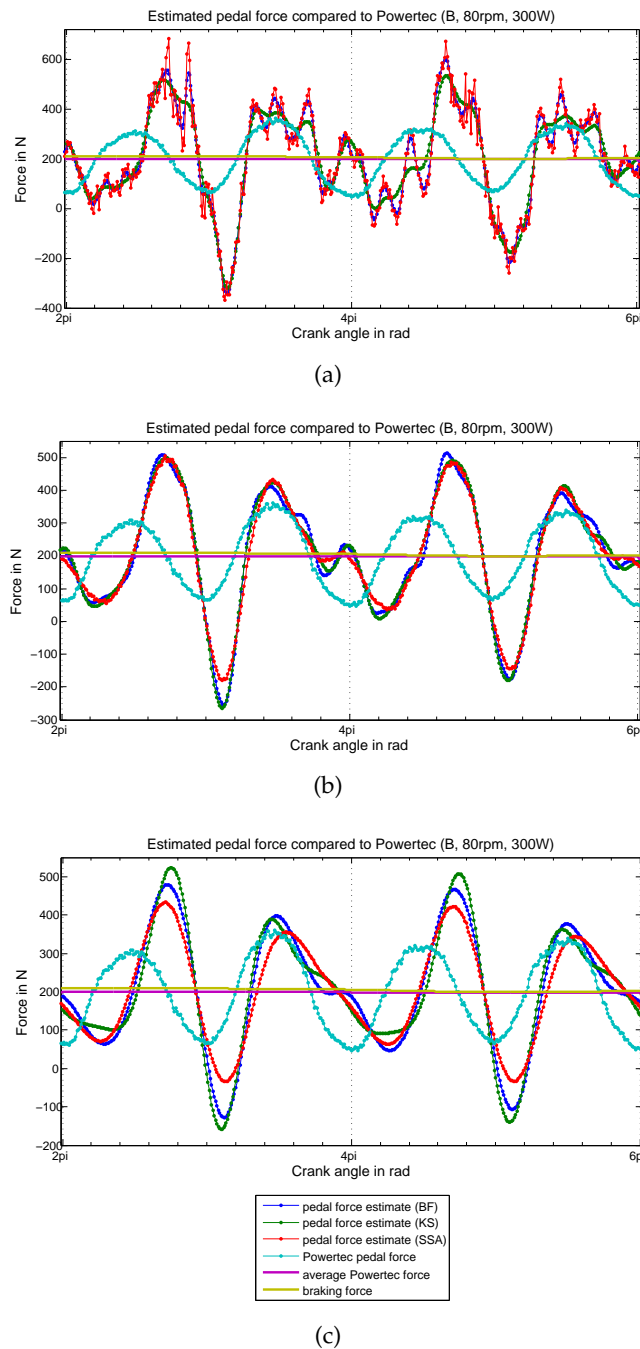


Figure 6.4: Estimated pedal force profiles are compared to respective Powertec pedal force. The degree of smoothing of the underlying position data was low in (a), medium in (b), and high in (c).

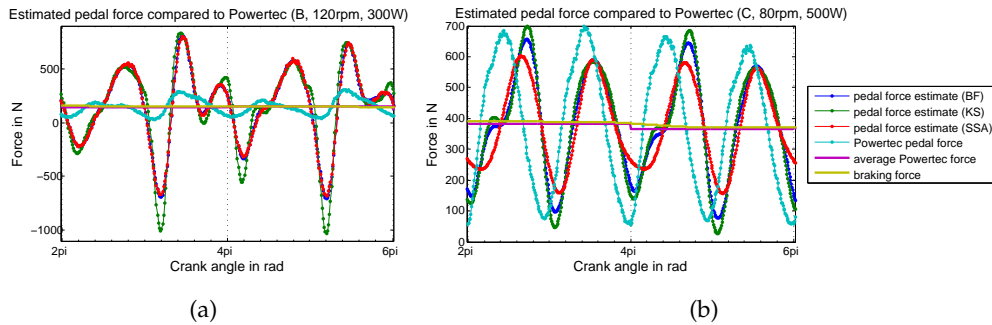


Figure 6.5: (a) shows the pedal force profiles of a measurement with a cadence of 120 rpm based on a medium amount of smoothing of the position data. In (b) the position data was filtered with a high degree of smoothing, and the amplitudes of the estimated pedal force are rather smaller than those of the Powertec pedal force.

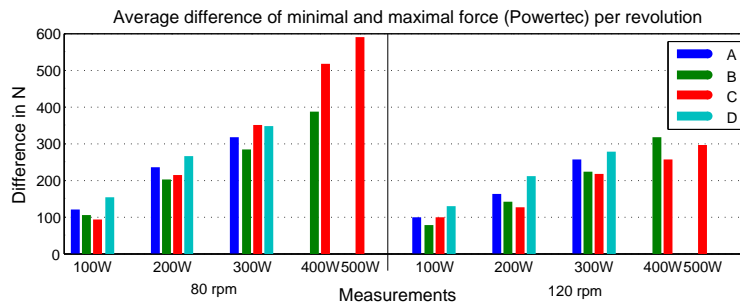


Figure 6.6: The average difference of minimal and maximal pedal force per revolution is shown for the 30 measurements.

### 6.2.1 Two Major Force Peaks

The computed pedal force clearly shows two force peaks per crank revolution as does the Powertec pedal force. However, for nearly all measurements the magnitude of those peaks is considerably larger than those of the Powertec pedal force.

For some measurements the amplitude of the estimated pedal force based on strongly smoothed data is smaller than that of the Powertec pedal force, but the shape of the force profile still differs significantly (see Figure 6.5(b)).

The differences between the obtained pedal force and the pedal force determined by Powertec becomes even worse for measurements with a cadence of 120 rpm (see Figure 6.5(a)).

As discussed in the last section, the amplitude (i.e., the difference between the minimum and maximum value within a pedal cycle) of the angular acceleration curve grows with ascending power and with ascending cadence (Figure 6.3). The amplitude of the pedal force measured with Powertec also grows

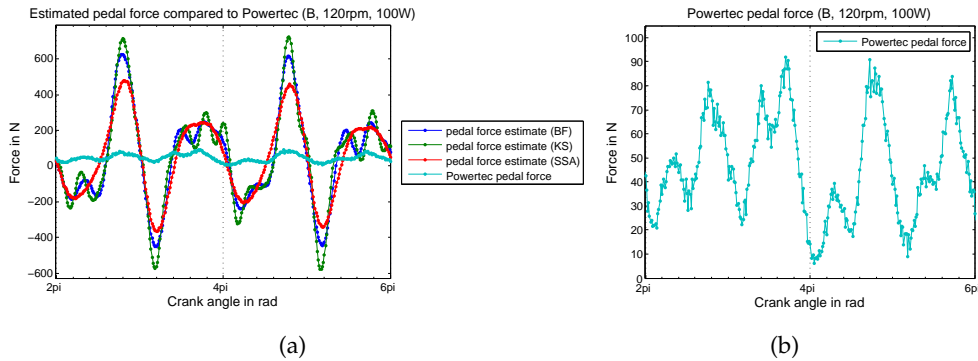


Figure 6.7: A pedal profile for a measurement with a cadence of 120 rpm and a power of 100 W is shown. In (a) the pedal force estimates were smoothed at a medium level. (b) zooms in, showing only the Powertec pedal force.

with ascending power. But in contrast to the angular acceleration, it descends for increasing cadence, as shown in Figure 6.6. Hence, pedal force estimates regarding measurements with a cadence of 120 rpm deviate stronger from the referential Powertec force than measurements at 80 rpm.

### 6.2.2 Further Minor Force Peaks

Besides the two major peaks the estimated pedal force shows further minor peaks. Most obvious is the minor peak occurring when the crank is at the bottom dead centre, resulting from the respective angular acceleration. In Figure 6.4 and 6.5 the Powertec pedal force does not show such a minor peak. Considering a measurement with high cadence (120 rpm) and low power (100 W) in Figure 6.7, the pedal force profile measured with Powertec reveals such minor peaks as well.

Generally, minor peaks in the Powertec pedal force profiles are the more pronounced the higher the cadence and the lower the power. For Powertec measurements at a cadence of 80 rpm slight minor peaks are perceptible at a power of 100 W, but not for higher power. Measurements of 120 rpm reveal minor peaks up to a power level of 300 rpm. Concluding, it can be observed that the lower the total force, the more clearly pronounced are the minor peaks in the Powertec measurements.

Regarding the Powertec measurements, those minor peaks occurring for small forces might be due to mechanical reasons. A possible reason might be that the flywheel temporarily runs at idle, caused by its high velocity and low resistive forces.

Moreover, it might have been some play in the bottom bracket. A somewhat loose bottom bracket probably would not influence the pedal force profiles if the pedal force is high. However, for a low pedal force the resistance of brake and flywheel are small as well. Then, the resistance provided by crank, and bottom bracket contributes stronger to the total resistance and a loose bottom bracket could cause peaks in the force profile.

Some play within the bottom bracket would influence the trajectory of the pedal marker, regardless of the power and cadence. Hence, this would explain minor peaks in pedal force profiles based on motion capturing, even if the respective Powertec profile does not reveal those peaks.

### 6.2.3 Braking Force

The braking force of the ergometer was assumed to be rather constant. In Section 2.2.3 it was argued that oscillations of the braking force due to changes of the flywheel's angular velocity within a pedal cycle play only a marginal role with respect to the total force.

Correcting the braking force for these possible variations did not result in significant changes of the pedal force estimates.

The braking force is a function of the angular velocity of the flywheel and the current supplied to it, and the major changes in braking force result from the amount of current which is supplied. To yield a rather constant power level the resistance is automatically adapted. It was assumed that these adaptations are smooth, hence providing a rather constant braking force.

Nonetheless, the possibility cannot be eliminated, that those changes in resistance occur much faster. In that case the braking force based on SRM measurements of average cadence and average power would not account for quick changes and deviate from the true braking force to some unknown extent.

### 6.2.4 Phase Lag

A phase lag exists between the profiles of the pedal force obtained by our method and that measured by Powertec. This might partly originate from a shift of a few degrees of the Powertec trigger. As reported by the Radlabor Freiburg, a slight shift of the Powertec trigger had been observed, but it could not be resolved if this shift was corrected before or after we carried out our measurements.

Marker *Trigger*, which was used to define the start of each crank revolution for the motion data, might have been slightly misplaced as well.

Further, the phase lag might result from possible incorrectness of the obtained angular acceleration, due to the ellipsoidal trajectory of the pedal marker.

# 7 Conclusions

In this concluding chapter, we want to summarise the main points of this thesis and give an outlook for related topics that might be in focus of future research.

## 7.1 Summary

This thesis deals with the force applied to the pedal in ergometer cycling. An approach was taken to compute pedal force based on the braking force of the ergometer and the moment of inertia of the ergometer's flywheel.

Braking force was obtained from the power and cadence measurements of the ergometer, whilst the proportion of the total pedal force which is due to the inertia of the flywheel was determined based on the angular acceleration of the crank.

The crank angle was obtained with a motion capture system by tracking the movement of a marker placed on the pedal axis. Then the angular acceleration of the crank was calculated as the second derivative of the crank angle.

The computation of the crank angular acceleration was faced with two major problems, which were extensively discussed in Chapter 5 and 6. One was the general problem of computing derivatives of noisy measurement data. The other was the ellipsoidal trajectory of the pedal marker that raised doubts whether the obtained crank angles resemble the true crank angles.

The issue of computing derivatives of noisy measurements was met by smoothing the measurement data beforehand. Three smoothing techniques (a Butterworth filter, a Kalman smoother, and singular spectrum analysis) and three degrees of smoothing were applied. A solution regarding the ellipsoidal pedal marker trajectory could not be found.

The pedal force obtained differed considerably from the pedal force measured by the Powertec System, regardless of the smoothing technique and the amount of smoothing. Thus, at the current status the method proposed by this thesis cannot be advised for estimating pedal force.

Elements of uncertainty were identified, which are in particular the optimal amount of smoothing and the smoothing technique, and the trajectory of the pedal marker that deviated from a perfect circle. Resolving these open questions is seen as the starting point for obtaining better pedal force estimates.

An incorrectness of the fundamental assumptions made regarding the nature of pedal force in ergometer cycling cannot be excluded. However, a re-

lated approach was followed successfully by Lakomy [Lak93]. Two main differences existed in his method. He used a friction-loaded cycle ergometer, and he obtained acceleration by monitoring the flywheel speed with a small electric generator which was driven by the flywheel. Furthermore, he used different flywheel inertia, and power and cadence settings.

This leads to the assumption that our approach might be theoretically correct, but raises the question about the reasons for its practical failure. Hence, further research on this topic seems worthwhile.

## 7.2 Outlook

The experiments within this thesis were carried out only once. As the measurement devices used are not available at our university department, further iterations were not possible. Therefore, certain problems could not be resolved.

### Instrumental Error

The trajectory of the pedal marker was ellipsoidal instead of circular, and it could not be determined to what extent the computed crank angles were distorted due to this deviation. To correct the calculation of the crank angles further information is needed.

Placing an additional marker at the bottom bracket allows to capture the possibly moving axis of the crank rotation. At some stage of the pedal cycle, especially at the bottom dead centre, the foot/leg hides the marker on the bottom bracket, and no position data will be available. Anyhow, information about the crank position of the other parts of the pedal cycle could be used to approximate the hidden positions.

A second marker placed on the pedal permits, in combination with the marker on the pedal axis, to calculate the position of the pedal with respect to the crank or the circle around the bottom bracket. This helps to investigate whether the deviations of the pedal marker depend on the angle between pedal and crank, which changes throughout the pedal cycle. In that case the additional information could be used to approximate the correct crank angles.

Moreover, it was pointed out in Section 6.2.2 that a loose bottom bracket might be a major problem for the pedal force estimation. Hence, the bottom bracket should be tightened prior to the experiments.

### Measurement Noise

For optimal filtering of noisy measurement data, which is a prerequisite to obtain proper derivatives, knowledge of the characteristics of the noise is beneficial. In this thesis, only the noise of the markers on the floor could be analysed, as the pedal marker was solely captured while moving. However, the measurement noise can vary for different spatial positions.

For further studies it is proposed to capture the data of the pedal marker at several crank angles while standing motionless. Analysing the respective noise would be valuable to decide whether a filtering technique based on non-Gaussian or non-white noise is more appropriate than the techniques used within this thesis.

The motion data of the markers of the floor showed irregularities (e.g., a slight movement although the markers were fixed on the ground) that could not be explained with certainty (see Section 5.1.1). Maybe this could be diminished by recalibrating the LUKOtronic system in between the single measurements.

Even if information about the noise affecting the measurements is available, uncertainty remains about the correctness of the obtained derivatives of smoothed motion data. Commonly researchers evaluate estimation of second derivatives by measuring acceleration simultaneously by means of an accelerometer, or they use synthetic data whose true derivatives are known.

It is essential to measure the true angular acceleration of the crank (e.g., by using an accelerometer) to find out if the failure of our approach is due to the problem of derivative computation of noisy data.

Moreover, the accelerometer could be used as a guide for subsequent smoothing, by making use of the information it provides about the frequency distribution and the noise level [RXC<sup>+</sup>06].

However, Ladin and Wu found that force estimates based solely on position measurements are less accurate than those involving accelerometers [LW91]. They suggest that accelerometers are necessary to accurately measure segmental acceleration for physical activities faster than slow walking, due to high frequency components contained within the data.

To filter non-stationary data (i.e., data that also contains higher frequencies at certain stages throughout the motion) joint time-frequency domain analysis methods like the Wigner Function [GSV00, GSG02] promise better result than techniques working either within time or within frequency domain. Hence such a technique might yield more appropriate acceleration estimates.

Based on the recommendations made above, further research is needed to find out a) if the method proposed by this thesis works in case the true angular acceleration of the crank is available (i.e., by using an accelerometer), and b) whether sufficiently correct estimates of the crank angular acceleration can be obtained using motion capturing.

# List of Figures

2.1	Components of force applied to the pedal . . . . .	7
2.2	Resultant force and pedal orientation . . . . .	7
2.3	Crank torque profiles . . . . .	8
2.4	Propagation of pedal force . . . . .	9
2.5	Outline of force propagation from pedal to flywheel . . . . .	11
2.6	Constant and varying braking force . . . . .	12
3.1	Reconstruction of marker position . . . . .	15
3.2	Camera and markers of LUKOtronic System . . . . .	16
3.3	Powertec System mounted on SRM Training System . . . . .	17
3.4	Setup of measuring instruments and coordinate system . . . . .	18
4.1	Outline of pedal force computation . . . . .	22
5.1	Variation of mean positions of floor markers . . . . .	28
5.2	Movement of a markers position during recording . . . . .	29
5.3	Motion of marker <i>Marker3</i> . . . . .	30
5.4	Motion of marker <i>Origin</i> . . . . .	30
5.5	<i>Trigger</i> noise with and without outliers . . . . .	31
5.6	Correlation of <i>Trigger</i> outliers and crank angle . . . . .	31
5.7	Histograms of floor markers . . . . .	34
5.8	Autocorrelation functions of floor marker noise . . . . .	35
5.9	Variance of noise . . . . .	36
5.10	Motion of pedal marker with regards to outliers and NaNs . . . . .	37
5.11	Ellipsoidal motion of pedal marker . . . . .	38
5.12	Radius of fitted ellipse . . . . .	39
5.13	Three-dimensional motion of the pedal ( <b>pedal3D</b> ). . . . .	41
5.14	Pedal position data before and after preprocessing . . . . .	41
5.15	Non-smoothed translational and angular velocity and acceleration . . . . .	43
5.16	Amplitude spectrum of pedal position data . . . . .	44
5.17	Amplitude spectrum floor marker . . . . .	45
5.18	Function for automatic determination of cutoff frequency . . . . .	46
5.19	Residuals for Butterworth filter . . . . .	47
5.20	Singular spectrum . . . . .	54
5.21	Computation of crank angle . . . . .	55
6.1	Position data before and after smoothing . . . . .	59
6.2	Crank angular velocity and acceleration profiles . . . . .	60
6.3	Amplitude of angular velocity and acceleration . . . . .	61

---

6.4	Pedal force profiles (cadence 80rpm, power 300W) . . . . .	62
6.5	Pedal force profiles (cadence and power: 120rpm, 300W, and 80rpm, 500W) . . . . .	63
6.6	Amplitude of Powertec pedal force . . . . .	63
6.7	Pedal force profile (cadence 120rpm, power 100W) . . . . .	64

# Bibliography

- [AB74] R. S. Anderssen and P. Bloomfield. Numerical differentiation procedures for non-exact data. *Numer. Math.*, 22:157–182, 1974.
- [ADCP04] F. J. Alonso, J. M. Del Castillo, and P. Pintado. An automatic filtering procedure for processing biomechanical kinematic signals. In Barreiro et. al., editor, *ISBMDA 2004, LNCS 3337*, pages 281–291. Springer, 2004.
- [ADCP05] F. J. Alonso, J. M. Del Castillo, and P. Pintado. Application of singular spectrum analysis to the smoothing of raw kinematic signals. *J. Biomech.*, 38:1085–1092, 2005.
- [AS97] M. R. Allen and L. A. Smith. Optimal filtering in singular spectrum analysis. *Physics Letters A*, 234(6):419–428, 1997.
- [AV96] G. Alvarez and J. Vinyolas. A New Bicycle Pedal Design for On-Road Measurements of Cycling Forces. *J. Appl. Biomech.*, 12(1):130–142, 1996.
- [BG90] J.P. Broker and R.J. Gregor. A dual piezoelectric element force pedal for kinetic analysis of cycling. *Int. J. Sports Biomech.*, 6:394–403, 1990.
- [BG96] J. P. Broker and R. J. Gregor. Cycling Biomechanics. In E. R. Burke, editor, *High-Tech Cycling*. Human Kinetics, Champaign IL, 1996.
- [Bro03] J.P. Broker. Cycling Biomechanics: Road and Mountain. In E. R. Burke, editor, *High-Tech Cycling*. Human Kinetics, Champaign IL, 2nd edition, 2003.
- [CFL93] M. L. Corradini, S. Fioretti, and T. Leo. Numerical differentiation in movement analysis: how to standardise the evaluation of techniques. *Med. Biol. Eng. Comput.*, 31(2):187–197, 1993.
- [Cha99] J. H. Challis. A procedure for the automatic determination of filter cutoff frequency for the processing of biomechanical data. *J. Appl. Biomech.*, 15:303–317, 1999.
- [Cha08] J. H. Challis. Data processing and error estimation. In C. J. Payton and R. M. Bartlett, editors, *Biomechanical evaluation of movement in sport and exercise: the British Association of Sport and Exercise Sciences guidelines*, chapter 7, pages 129–152. Routledge, London ; New York, 2008.
- [CS86] P. Cavanagh and D. Sanderson. The biomechanics of cycling: Studies of the pedaling mechanics of elite pursuit riders. In

- E. R. Burke, editor, *Science of Cycling*, chapter 5. Human Kinetics, Champaign IL, 1986.
- [DF92] M. D'Amico and G. Ferrigno. Comparison between the more recent techniques for smoothing and derivative assessment in biomechanics. *Med. Biol. Eng. Comput.*, 30(2):193–204, 1992.
- [DPCMS79] P.E. Di Prampero, G. Cortili, P. Mognoni, and F. Saibene. Equation of motion of a cyclist. *J. Appl. Physiol.*, 47(1):201–206, 1979.
- [EJG<sup>+</sup>07] L. M. Edwards, S. A. Jobson, S. R. George, S. H. Day, and A. M. Nevill. The effect of crank inertial load on the physiological and biomechanical responses of trained cyclists. *J. Sports Sci.*, 25(11):1195–1201, September 2007.
- [FC78] I. E. Faria and P. R. Cavanagh. *The physiology and biomechanics of cycling*. American College of Sports Medicine Series. Wiley, New York, 1978.
- [FJ89] S. Fioretti and L. Jetto. Accurate derivative estimation from noisy data: A state-space approach. *Int. J. Syst. Sci.*, 20(1):33–53, 1989.
- [FJ94] S. Fioretti and L. Jetto. Low a priori statistical information model for optimal smoothing and differentiation of noisy signals. *Int. J. Adaptive Cont. Signal Proc.*, 8(4):305–320, 1994.
- [FZD96] B. J. Fregly, F. E. Zajac, and C. A. Dairaghi. Crank inertial load has little effect on steady-state pedaling coordination. *J. Biomech.*, 29(12):1559–1567, 1996.
- [GA08] M. S. Grewal and A. P. Andrews. *Kalman Filtering. Theory and Practice using MATLAB*. John Wiley & Sons, 3rd edition, 2008.
- [GB97] G. Giakas and V. Baltzopoulos. Optimal digital filtering requires a different cut-off frequency strategy for the determination of the higher derivatives. *J. Biomech.*, 30(8):851–855, 1997.
- [GBR91] R. J. Gregor, J. P. Broker, and M.M. Ryan. The biomechanics of cycling. *Exercise and Sport Sciences Reviews*, 19:127–169, 1991.
- [Gel74] A. Gelb, editor. *Applied Optimal Estimation*. MIT Press, 1974.
- [Ger04] M. S. Geroch. Motion capture for the rest of us. *J. Comput. Small Coll.*, 19(3):157–164, 2004.
- [GNZ01] N. Golyandina, V. Nekrutkin, and A. Zhigljavsky. *Analysis of Time Series Structure: SSA and related techniques*. Chapman and Hall/CRC, 2001.
- [Grü04] D. C. von. Grünigen. *Digitale Signalverarbeitung mit einer Einführung in die kontinuierlichen Signale und Systeme*. Fachbuchverlag Leipzig im Carl-Hanser Verlag, München, 3rd edition, 2004.
- [Gre05] M. Gressmann. *Fahrradphysik und Biomechanik. Technik, Formeln, Gesetze*. Delius Klasing Verlag, Bielefeld, 9th edition, 2005.

- [GSG02] A. Georgakis, L. K. Stergioulas, and G. Giakas. Automatic algorithm for filtering kinematic signals with impacts in the wigner representation. *Med. Biol. Eng. Comput.*, 40(6):625–633, 2002.
- [GSV00] G. Giakasa, L. K. Stergioulas, and A. Vourdas. Time-frequency analysis and filtering of kinematic signals with impacts using the wigner function: accurate estimation of the second derivative. *J. Biomech.*, 33(5):567–574, 2000.
- [Hat81] H. Hatze. The use of optimally regularized fourier series for estimating higher-order derivatives of noisy biomechanical data. *J. Biomech.*, 14:13–18, 1981.
- [HD81] M.L. Hull and R.R. Davis. Measurement of pedal loading in bicycling: I. instrumentation. *J. Biomech.*, 14(12):843–856, 1981.
- [HMH01] T. Henke, C. Monfeld, and H. Heck. Trettechnik - Einzelzyklusdarstellung im Radsport. In Bundesinstitut für Sportwissenschaft, editor, *BISp-Jahrbuch 2001*, pages 127–144. BISp, Köln, 2001.
- [HSS<sup>+</sup>98] M. Hillebrecht, A. Schwirtz, B. Stapelfeldt, W. Stockhausen, and M. Bührle. Trittechnik im Radsport: Der "runde Tritt" - Mythos oder Realität. *Leistungssport*, 28(6):58–62, 1998.
- [HZ04] R.I. Hartley and A. Zisserman. *Multiple View Geometry in Computer Vision*. Cambridge University Press, 2nd edition, 2004.
- [IA99] A. R. Ismaila and S. S. Asfour. Discrete wavelet transform: a tool in smoothing kinematic data. *J. Biomech.*, 32(3):317–321, 1999.
- [Jäh91] B. Jähne. *Digitale Bildverarbeitung*. Springer, 2 edition, 1991.
- [Kyl86] C. K. Kyle. Mechanical factors affecting the speed of a cycle. In E. R. Burke, editor, *Science of Cycling*. Human Kinetics, Champaign, IL, 1986.
- [Lak93] H. K. A. Lakomy. An indirect method for measuring the torque applied to friction-loaded cycle ergometers. *Ergonomics*, 36(5):489–496, 1993.
- [LRS86] M. M. Lavrent'ev, V. G. Romanov, and S. P. Shishatskiĭ. *Ill-posed problems of mathematical physics and analysis*, volume 64 of *Translations of Mathematical Monographs*. American Mathematical Society, 1986.
- [LUK] Lutz-Kovacs-Electronics LUKOtronic. *LUKOtronic Motion Analysis System AS 200. SYSTEM DESCRIPTION*.
- [LW91] Z. Ladin and G. Wu. Combining position and acceleration measurements for joint force estimation. *J. Biomech.*, 24(12):1173–1187, 1991.
- [May79] P. S. Maybeck. *Stochastic models, estimation, and control Vol. 1*. Mathematics in Science and Engineering. Academic Press, 1979.

- 
- [Men00] A. Menache. *Understanding Motion Capture for Computer Animation and Video Games*. Morgan Kaufmann Publishers Inc., San Diego, CA, 2000.
- [NHZ88] J. Newmiller, M. L. Hull, and F. E. Zajac. A mechanically decoupled two force component bicycle pedal dynamometer. *J. Biomech.*, 21(5):375–386, 1988.
- [Nie94] Y. Nievergelt. Total least squares: State-of-the-art regression in numerical analysis. *SIAM Review*, 36(2):258–264, 1994.
- [Par02] R. Parent. *Computer Animation. Algorithms and Techniques*. Morgan Kaufmann Publishers Inc., San Francisco, CA, USA, 2002.
- [PNW77] J. C. Pezzack, R. W. Norman, and D. A. Winter. An assessment of derivative determining techniques used for motion analysis. *J. Biomech.*, 10:377–382, 1977.
- [RXC<sup>+</sup>06] S. Rahmatalla, T. Xia, M. Contratto, D. Wilder, L. Frey-Law, G. Kopp, and N. Grosland. 3d displacement, velocity, and acceleration of seated operators in whole body vibration environment using optical motion capture systems. *The Ninth International Symposium on the 3-D Analysis of Human Movement in Valenciennes (France)*, 2006.
- [SMO<sup>+</sup>07] B. Stapelfeldt, G. Mornieux, R. Oberheim, A. Belli, and A. Gollhofer. Development and evaluation of a new bicycle instrument for measurements of pedal forces and power output in cycling. *Int. J. Sports Med.*, 28(4):326–332, 2007.
- [Sta06] B. Stapelfeldt. Biomechanische Messmethodik im Radsport. In K. Witte, J. Edelmann-Nusser, A. Sabo, and E. F. Moritz, editors, *Sporttechnologie zwischen Theorie und Praxis IV*, pages 319–327. Shaker Verlag, Aachen, 2006.
- [Ste04] N. Stergiou. *Innovative Analyses of Human Movement*. Human Kinetics, Champaign, IL, 2004.
- [Wil04] D. G. Wilson. *Bicycling Science*. MIT Press, 3 edition, 2004.
- [Win90] D. A. Winter. *Biomechanics and Motor Control of Human Movement*. John Wiley & Sons, New York, 2nd edition, 1990.
- [Wol85] H. J. Woltring. On optimal smoothing and derivative estimation from noisy displacement data in biomechanics. *Human Movement Science*, 4:229–245, 1985.
- [Wol86] H. J. Woltring. A fortran package for generalized, cross-validatory spline smoothing and differentiation. *Adv. Eng. Software*, 8(2):104–113, 1986.
- [Wol95] H. J. Woltring. Smoothing and differentiation techniques applied to 3-d data. In P. Allard, I. A. F. Stokes, and J. P. Blanchi, editors, *Three-dimensional analysis of human movement*, pages 79–99. Human Kinetics, Champaign, IL, 1995.

- 
- [Woo06] A. Wooles. Srm user manual. online option & ergometer., 2006. [http://www.srm.de/Software/Ergometer\\_English.pdf](http://www.srm.de/Software/Ergometer_English.pdf) [Accessed 02. Decembre 2008].
- [Woo07] A. Wooles. Srm user manual, 2007. [http://www.srm.de/Software/SRMManual\\_English.pdf](http://www.srm.de/Software/SRMManual_English.pdf) [Accessed 20. Octobre 2008].
- [WSH74] D. A. Winter, H. G. Sidwall, and D. A. Hobson. Measurement and reduction of noise in kinematics of locomotion. *J. Biomech.*, 4:157–159, 1974.
- [You37] G. Young. Matrix approximations and subspace fitting. *Psychometrika*, 2(1):21–25, 1937.